Taylor & Francis
Taylor & Francis Group

Mechanics Based Design of Structures and Machines

An International Journal

ISSN: (Print) (Online) Journal homepage: https://www.tandfonline.com/loi/lmbd20

Fluid-structure interaction analysis of a lightweight sandwich composite structure for solar central receiver heliostats

Sulaiman O. Fadlallah, Timothy N. Anderson & Roy J. Nates

To cite this article: Sulaiman O. Fadlallah, Timothy N. Anderson & Roy J. Nates (2022): Fluid-structure interaction analysis of a lightweight sandwich composite structure for solar central receiver heliostats, Mechanics Based Design of Structures and Machines, DOI: 10.1080/15397734.2021.2011744

To link to this article: https://doi.org/10.1080/15397734.2021.2011744

Published online: 31 Jan 2022.

MECHANICS BASED DESIGN OF STRUCTURES AND MACHINES
https://doi.org/10.1080/15397734.2021.2011744

Fluid-structure interaction analysis of a lightweight sandwich composite structure for solar central receiver heliostats

Sulaiman O. Fadlallah[a], Timothy N. Anderson[b], and Roy J. Nates[b]

[a]School of Computing and Engineering, University of Huddersfield, Huddersfield, UK; [b]Department of Mechanical Engineering, Auckland University of Technology, Auckland, New Zealand

ABSTRACT

Central tower concentrating solar power systems are moving to the forefront to become the technology of choice for generating renewable electricity, but their widespread implementation is limited by cost. Heliostats contribute almost 50% to the plant's cost and are thus the most significant element in central tower systems. For both large and small-area heliostats, the drive elements demonstrate the largest cost element in these systems. While large-area heliostats ($>100\,m^2$) have proven offer the best economy compared to other sizes, they require high-torque drives due to the heavy steel-based support structure. Heliostat costs could be reduced by decreasing the support structure's weight, avoiding large drive units and reducing energy consumption. However, the structure must be able to cope with the aerodynamic loads imposed upon them during operation. Although honeycomb sandwich composites have been widely used where high structural rigidity and low weight are desired, there is an absence of studies that rigorously investigated their suitability as the structure for heliostat mirror. Here, a fluid-structure interaction study investigated, for several loading conditions at various tilt and wind incidence angles, the aero-structural behavior characteristics of honeycomb sandwich composites used as a heliostat support structure. The honeycomb sandwich panel showed markedly different behavior characteristics at various operational conditions. The effect of tilt orientation on the sandwich panel's maximum deflection and stresses became more pronounced as wind velocity increased above 10 m/s, and increasing wind incidence angle reduced their magnitudes at different rates. The supporting components and torque tube had a noticeable wind-shielding effect, causing pronounced changes in the deflection and stresses experienced by the heliostat. The worst operational condition was at a tilt angle of 30° with wind flow of 20 m/s at 0° to the heliostat surface. However, the heliostat maintained its structural integrity according to relevant optical and material failure standards.

ARTICLE HISTORY
Received 23 March 2021
Accepted 22 November 2021

KEYWORDS
Heliostat; lightweight; sandwich composite; honeycomb; fluid-structure interaction

1. Introduction

Of all the renewable technologies available today for large-scale electricity production, central tower concentrating solar power (CSP) systems are marching to the forefront as they have the capability to become the technology of choice for the generation of renewable electricity (Behar,

CONTACT Sulaiman O. Fadlallah s.o.fadlallah@hud.ac.uk School of Computing and Engineering, University of Huddersfield, Huddersfield, UK.
Communicated by Nickolay Banichuk.

Khellaf, and Mohammedi 2013). Central tower CSP systems consist of a field of flat mirrors, also known as heliostats, that track the sun along two axes and reflect and concentrate the solar beam radiation onto a central receiver located at the top of a large tower. The receiver heats up and transmits heat to a heat transfer fluid that is then gets pumped down to conventional thermal power generation systems for electricity production. Central tower CSP systems can achieve high operating temperatures of the order of 1000 °C or even higher, qualifying these systems for thermal electric power production in the range of 10–1000 MW (Goswami 2015).

The potential for solar central tower systems to achieve high temperatures offers a path to higher efficiencies, thereby providing an inherent advantage over other CSP systems (i.e., Linear Fresnel, parabolic troughs, parabolic dishes). However, achieving these high temperatures requires a large number of heliostats. A 100 MW central tower power plant would require nearly one million square meters of glass heliostats, corresponding to approximately 10,000, 100 m^2 heliostats (Mancini 2000). Due to this large number of reflectors, heliostats represent the largest cost element in central tower CSP systems: almost 50% of the plant's total cost (Kolb et al. 2007). This has encouraged the development of innovative heliostat designs and solutions, aimed at reducing heliostats' cost without affecting their tracking performance, to enable the cost of energy from central tower plants to be competitive with fossil fuels (Mancini 2000; Pfahl et al. 2017).

Amongst the major components of a typical heliostat (reflective mirror module, back support structure, drive, torque tube and pedestal), for both large and small-area heliostats, the drive element (the component that rotates the structure to direct solar irradiation to the specified point location) has the greatest effect on heliostat production costs (Kolb et al. 2011), contributing approximately 30% of the total cost of small heliostats and approximately 27% of large ones. For large-area heliostats (>100 m^2), because of the heavy mirror support structure that is generally designed from steel, these reflectors require a high-torque drive. Kolb et al. provided a relationship between the drive's torque capacity and the heliostat's drive cost (Kolb et al. 2007). It was found that the torque capacity has a substantial impact on the drive cost and, so a promising opportunity arises for reducing the cost of heliostats by reducing the support structure's total weight while maintaining the heliostat's tracking performance and rigidity. Achieving this target requires a reduction in the amount of steel in the heliostat support structure and the use of stiff, lightweight materials.

This need for lightweight structures has raised the possibility of using advanced materials such as sandwich composites (Alijani and Amabili 2013). Sandwich composites are a possible solution due to their lightweight properties and high flexural stiffness (Heimbs et al. 2008; Ayub et al. 2011; Lande and Patil 2015; Cheng, Qiao, and Chen 2016). This type of composite is frequently utilized in the motorsport, construction, marine and aerospace industries (Birman and Kardomateas 2018; Li et al. 2021; Palomba, Epasto, and Crupi 2021; Redmann et al. 2021; Shifa, Tariq, and Chandio 2021) (applications where reducing weight, whilst sustaining the stiffness, is of key importance). The attractiveness of such materials lies in their comparatively low cost, high strength to weight ratio, corrosion resistance, energy absorbing capabilities (Paik, Thayamballi, and Kim 1999; Heimbs et al. 2008; Castellon 2012; Cheng, Qiao, and Chen 2016) and good damping characteristics. As such they have been the subject of much investigation, both numerically (Alijani and Amabili 2013) and experimentally (Alijani et al. 2013).

Sandwich composites consist of a lightweight core sandwiched between two thin facing layers using a strong adhesive. The core is produced from thick, lightweight materials able to withstand normal and shear loads (Zenkert 1997) and are typically made of high-strength materials, as the faces handle both compressive and tensile loads due to bending. For such composites a honeycomb-shaped core has been commonly utilized as the voids enable mass reduction while preserving stiffness. In addition, various properties can be obtained with simple variations in the honeycomb's geometrical configuration (e.g., cell wall angle, cell wall length and cell wall thickness), making them an excellent substitute for conventional isotropic materials in high performance engineering applications (Alijani and Amabili 2013).

The notable amount of work that has been done to test the mechanical properties and to understand the behavior of honeycomb sandwich panels under different loading conditions (i.e., in-plane (parallel to the surface), out-of-plane (normal to the surface)) (Yamashita and Gotoh 2005; Hu, You, and Yu 2011; Ivañez, Fernandez-Cañadas, and Sanchez-Saez 2017; Baumgart et al. 2018; Balaji and Annamalai 2019), along with the various sensitive applications that involved these materials, clearly reflects their potential to be utilized as the basis for a heliostat mirror structure.

1.1. Overview and contribution

Heliostats are exposed to the atmospheric conditions prevailing on the field. They experience aerodynamic forces caused by wind that can lead to structural deformations, affecting their optical performance. One of the challenges faced in implementing such systems is ensuring that they are able to cope with these aerodynamic loads imposed upon them. Although much research has been devoted to investigating the aerodynamic loads encountered by heliostats (Peterka et al. 1986; Peterka and Derickson 1992; Wu et al. 2010; Pfahl, Buselmeier, and Zaschke 2011; Emes et al. 2017), there is a dearth of studies investigating the suitability of honeycomb sandwich composites in heliostat mirror support structures. Moreover, despite very few attempts found in literature that utilized sandwich composites but with different core materials and configurations (Diver and Grossman 1998; Aldaz et al. 2018; Liedke et al. 2018), they did not investigate in great detail the interaction between the wind and sandwich composites employed as a heliostat mirror support structure.

Furthermore, these earlier investigations also lacked details concerning material properties, considered only small-area heliostats (in particular, $8\,m^2$ size in Aldaz et al. (2018) and $9\,m^2$ size in Liedke et al. (2018)) and did not take into account large-area heliostats ($>100\,m^2$). Hence, given the opportunity to reduce heliostats' cost by minimizing the total weight of the structure, and the fact that heliostats are sensitive to wind loads, there is a need for a better understanding of how honeycomb sandwich composites respond under wind effects when utilized as the support structure for a heliostat mirror.

The current study investigates the suitability of honeycomb sandwich composites for use as heliostat mirror structure, aiming to deliver a better understanding of the interactions of these structures with wind forces by investigating their aero-structural behavior characteristics. The work presented will be a significant milestone in the quest to develop cheaper lightweight heliostats that are strong and capable of withstanding wind loads and other environmental conditions, and a major step on the way to move central tower CSP systems to the forefront to become the technology of choice for energy production. This critical factor will contribute to achieving multiple criteria of the Sustainable Development Goals (SDGs), including economic, environmental, and social aspects. In the long run, this will lead to reducing barriers and increasing acceptance of solar energy as an option to address the world's long-term energy needs.

2. Numerical setup

To investigate the aero-structural robustness and behavior characteristics of honeycomb sandwich composites when employed as a heliostat mirror support structure, it was decided to carry out a computational fluid-structure interaction (FSI) analysis. This approach has been successfully employed in a number of prior studies on the interaction of structures such as wind turbines and photovoltaic systems with wind (Lin, Dai, and Wu 2013; MacPhee and Beyene 2013; Wang, Quant, and Kolios 2016; Lee et al. 2017). It is considered an effective way, especially during the development stage, to explore and examine a variety of designs and modifications at real scale, as field and wind tunnel experiments are time-consuming and expensive to set up. Computational

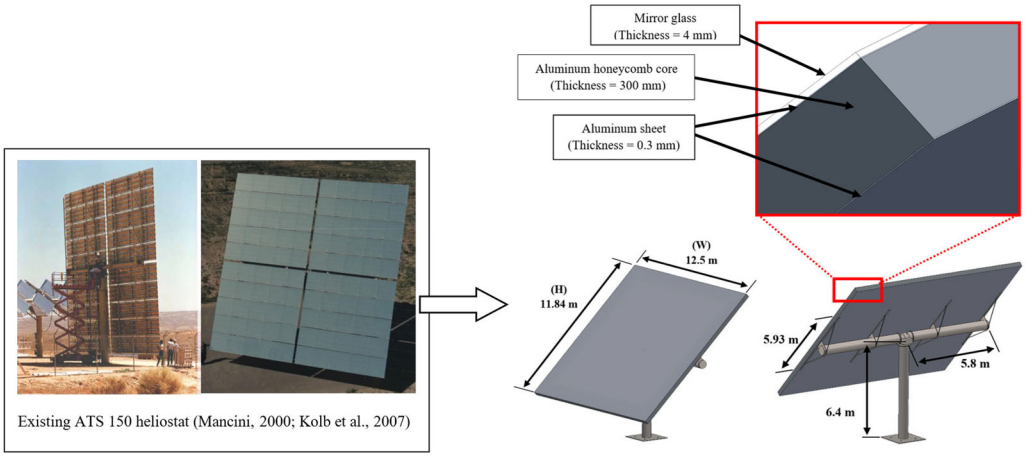

Figure 1. Sandwich composite-based heliostat geometrical configuration.

FSI analysis requires both aerodynamic and structural components to establish aerodynamic loads and the corresponding structural responses. Computational fluid dynamics (CFD) was chosen as the aerodynamic component of the computational FSI analysis. CFD is a powerful tool for obtaining reliable predicted aerodynamic forces on structures. It has been intensively utilized in heliostat studies (Wu et al. 2010; Marais, Craig, and Meyer 2015; Mammar et al. 2017; Aldaz et al. 2018) due to its flexibility when examining a diversity of heliostat designs and modifications and exploring their impact on the airflow around them (Bendjebbas, Abdellah-ElHadj, and Abbas 2016; Fadlallah, Anderson, and Nates 2021). For the structural component, due to its flexibility, high fidelity, and ability to examine detailed stress distributions within a structure (Wang, Quant, and Kolios 2016), finite element analysis (FEA) was selected.

Considering a typical heliostat configuration, which is an existing large-area steel-based heliostat manufactured by Advanced Thermal Systems (ATS) (Mancini 2000; Kolb et al. 2007), it was assumed that the heliostat would consist of a 148 m^2 (11.84 m (H) $\times$ 12.5 m (W)) rectangular sandwich composite plate (Figure 1). This size of reflector was chosen as a basis for this study, as Sandia National Laboratories' analysis of heliostat cost versus size (Kolb et al. 2007) indicated that heliostats of around 150 m^2 show the best economy. The sandwich composite plate is supported by four steel (Young's modulus (E) = 200 GPa; Poisson's ratio (v) = 0.3; Shear modulus (G) = 76.92 GPa; Density (ρ) = 7850 kg/m^3) attachments, each about 6 m long and 0.15 m wide. Unlike the ATS heliostat where the steel-based trusses extend along the entire reflector, the attachments were made smaller to reduce the amount of steel, since the sandwich panel should provide the mirror module with the necessary rigidity and support without fully relying on the heavy, steel-based support structure. For a detailed analysis of the attachments' size selection see Appendix A. Both the panel and the attachments are mounted on a steel-based torque tube/pedestal configuration, known as a T-type configuration (the torque tube and the pedestal together form a "T" and are coupled to each other by the drive system), selected because state-of-the-art central tower CSP plants mostly use T-type heliostats with azimuth-elevation tracking mechanisms (Téllez et al. 2014; Pfahl et al. 2017).

The heliostat's sandwich composite structure (Figure 1) was assumed to consist of a 300 mm aluminum honeycomb core sandwiched between two 0.3 mm aluminum skins. Aluminum (E = 69 GPa; v = 0.33; G = 27 GPa; ρ = 2700 kg/m^3) is the most widely used option for constructing honeycomb sandwich panels (Araújo et al. 2018) and has been extensively adopted in high performance engineering applications. The face sheets of these cores can be made of various metallic materials. Added to the ease of assembly, aluminum face sheets are preferred to be used with aluminum core, as they enable the structure to undergo large plastic deformations before

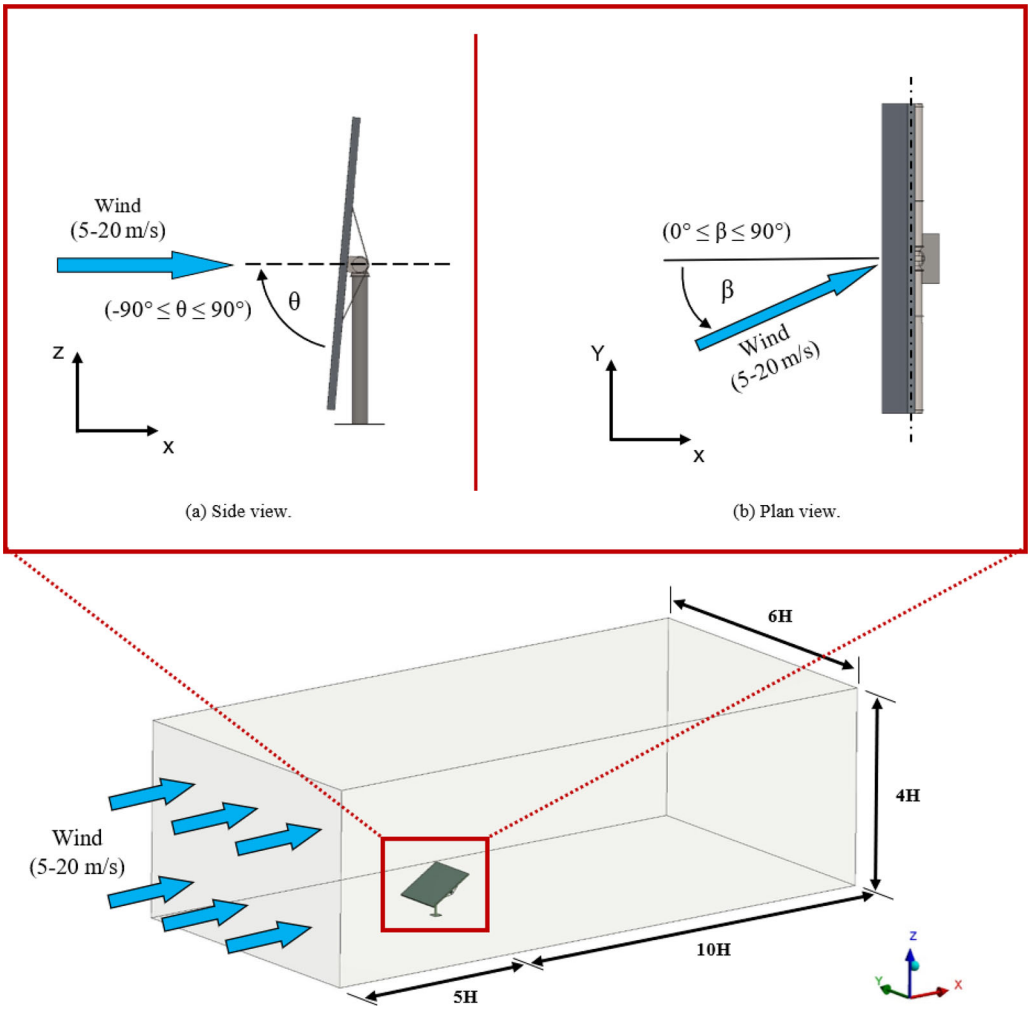

Figure 2. Computational domain of the CFD model and definition of tilt and wind incidence angles.

rupture due to aluminum's ductile nature (Jen and Chang 2009; Langdon et al. 2010; Çı nar 2014). Taking into account the heliostat's large reflective area and market availability, the selection of the sandwich panel's thickness was based on preliminary analysis carried out to determine an initial structural configuration that reduces the mirror support structure's total weight (in comparison to the existing 148 m^2 steel-based ATS heliostat's mirror support structure that weighs around 1550 kg, as reported by Kolb et al. (2007)), while maximizing its structural strength and robustness. A 4 mm thick glass mirror, similar to the one used in the ATS heliostat, was mounted on the top surface of the sandwich composite. Mirrored glass ($E = 68.94$ GPa; $v = 0.23$; $G = 28.02$ GPa; $\rho = 2457.6$ kg/m^3) was selected as the reflective surface, being relatively inexpensive, with a high reflectance (0.93–0.94) and durability (20–25 years' lifespan), and accepted by the industry in comparison to reflective films (Téllez et al. 2014; Pfahl et al. 2017). To accommodate differences in thermal expansion between the glass facets and the metallic support structure, mirrors are often connected to the support structure via flexible adhesives (Pfahl et al. 2017; Rumsey-Hill, Pottas, and Coventry 2019). However, for model simplification, the inclusion of this layer is neglected.

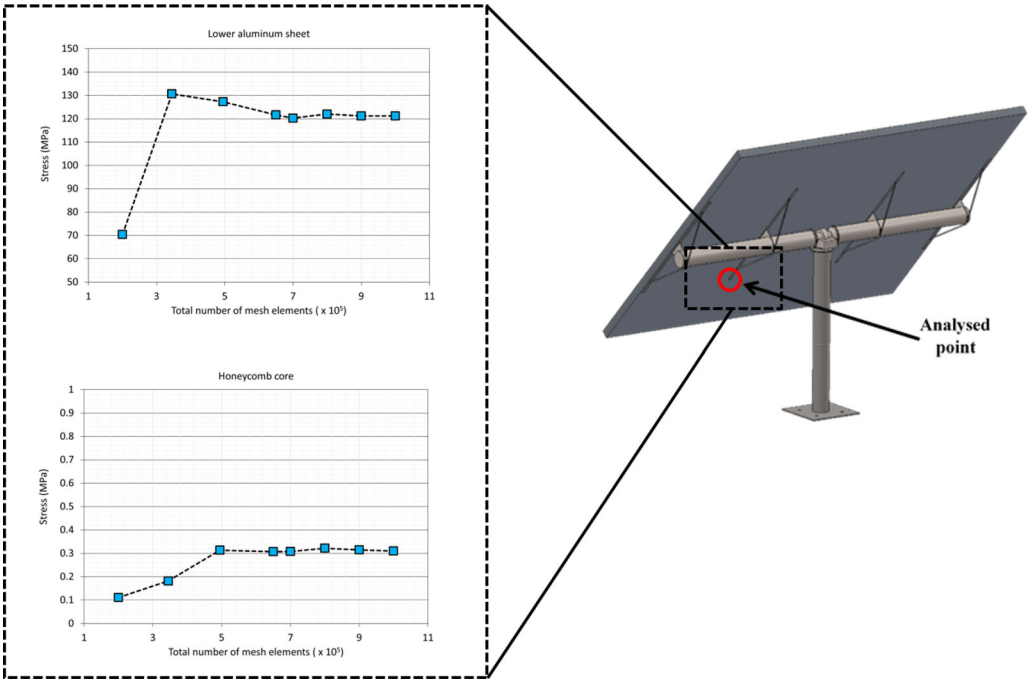

Figure 3. FEA mesh independence test.

In undertaking the FSI analysis, the wind (i.e., the aerodynamic component) flow around the heliostat was simulated utilizing the validated numerical CFD model reported in (Fadlallah, Anderson, and Nates 2021). A detailed description of the setup and its validation (i.e., mesh independence test, wind profile development, comparison with available data of wind loading coefficients) can be found therein. To determine the aerodynamic loads on the heliostat adequately, simulations were carried out for several wind incidence angles (β) between 0° to 90° and a range of tilt angles (θ) between 90° (wind flow perpendicular to the mirror surface) and −90° (wind impinging on the heliostat's back surface), with a wind velocity (V) range of 5–20 m/s (Reynolds number varying from 4.05×10^6 to 1.62×10^7 taking the chord length of the panel (H = 11.84 m) as the characteristic length) as shown in Figure 2.

To investigate the behavior characteristics of the honeycomb sandwich composite-based heliostat structure under wind loads, the predicted aerodynamic loads from the ANSYS/FLUENT CFD solver were then mapped to an FEA model of the heliostat developed in the ANSYS/Static Structural package. This coupling strategy is a one-way coupling method, which is less computationally intensive than the more complex unsteady two-way approach. In addition, obtaining and verifying the flow characteristics and aerodynamic loads is simpler but more reliable than with two-way FSI, where solution convergence and accurate results cannot be guaranteed (Wang, Quant, and Kolios 2016; Lee et al. 2017). For the FEA, an adaptive mesh was used to capture the behavior of all components (reflective mirror module, back support structure, drive, torque tube and pedestal). Different meshing techniques using shell and beam elements were explored and abandoned due to meshing complications stemming from complex geometries and interconnected parts. To accommodate these complications, 3 D solid 8-node hexahedral and 4-node tetrahedral elements were used to construct the FEA model. Fine meshes were generated to reduce any numerical instabilities when importing the aerodynamic loads from the CFD solver, and to ensure that the stress field around the steel attachment points is not singular.

Different grid sizes were tested to check their effects on the heliostat's recorded stress at a specified point, shown in Figure 3, when the structure is tilted at an angle of 30° and

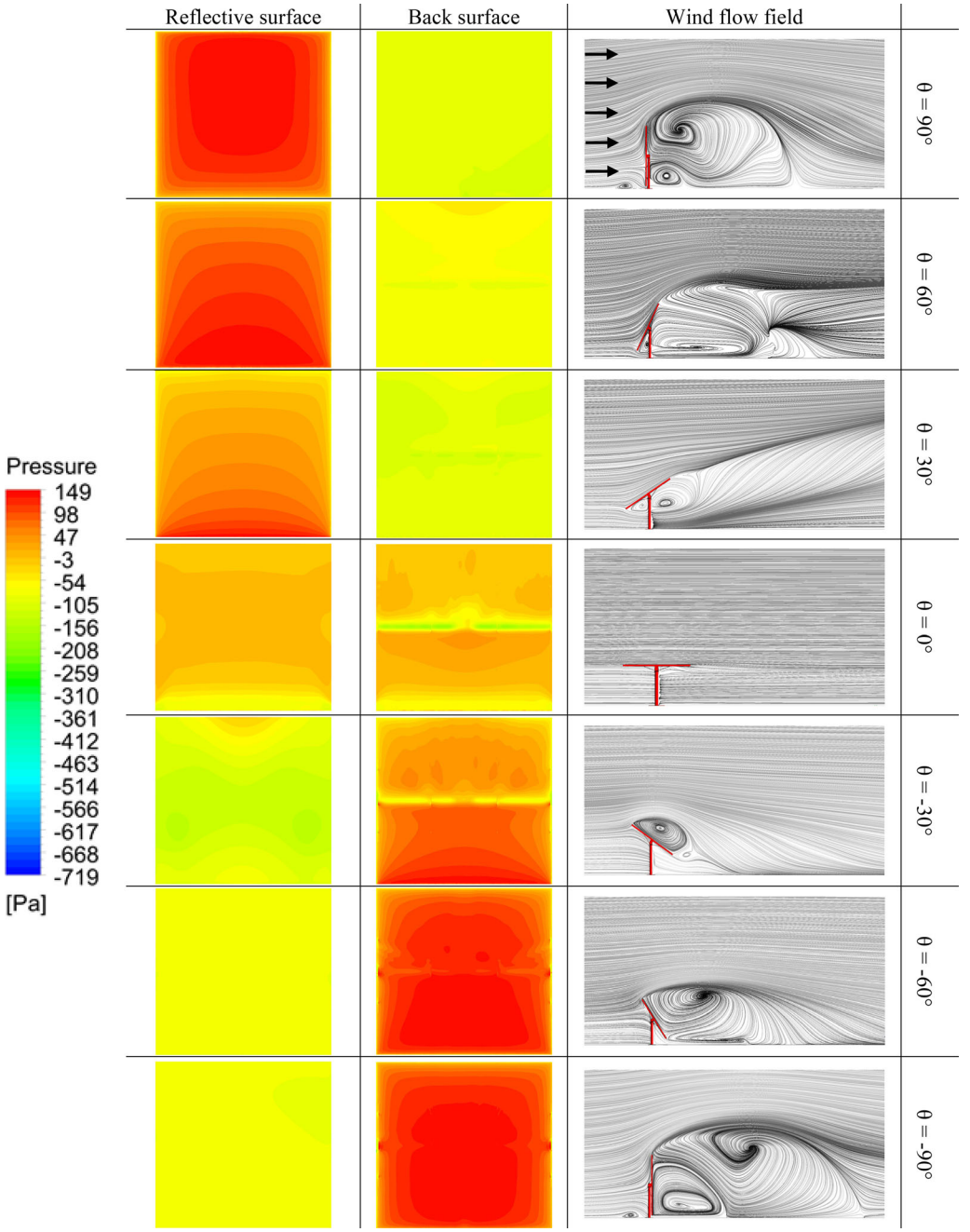

Figure 4. Pressure distribution on the heliostat at wind velocity of 15 m/s approaching at 0° incidence angle (β).

experiencing wind at 0° incidence angle with a velocity of 20 m/s. There was no significant change in the results with an increase in grid size beyond 650,000 elements; hence the computational mesh selected for further analysis consisted of approximately 650,000 elements distributed across the heliostat model, with boundary conditions set in a way similar to the operation conditions of the given heliostat. As the bottom of the heliostat is fixed on the ground, nodes on the bottom of the pedestal support were set to be fully constrained.

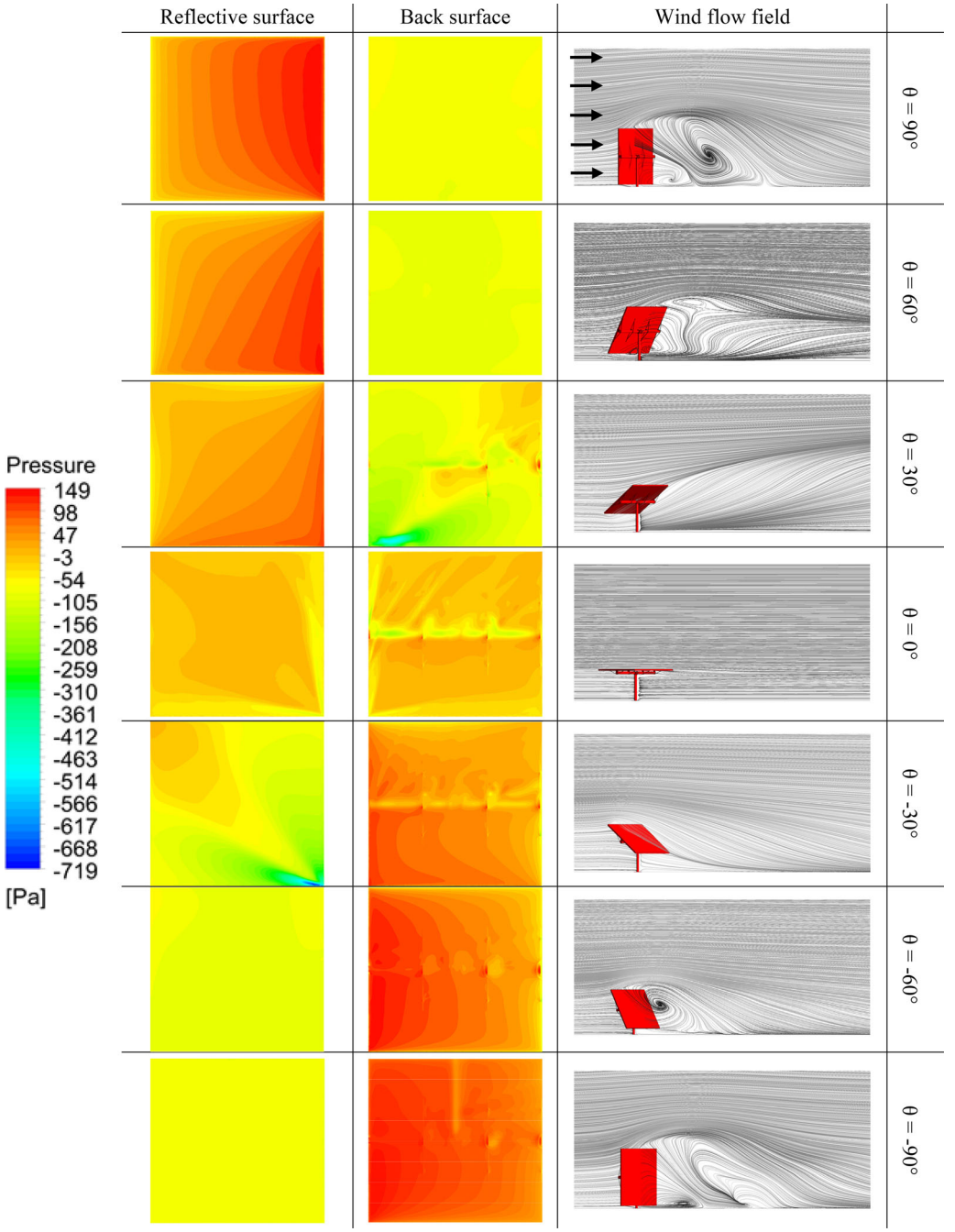

Figure 5. Pressure distribution on the heliostat at wind velocity of 15 m/s approaching at 45° incidence angle (β).

The face/adhesive/core junction was modeled as perfectly bonded with common nodes. The bottom face of the sandwich was connected using common nodes to the four steel attachments. Finally, the other contact surfaces in the heliostat model were assumed to be bonded such that the nodes of adjacent components would move together on each contact surface. Prior to thoroughly investigating the aero-structural behavior of the honeycomb sandwich composite-based heliostat, a linear and nonlinear static analysis was performed to compare the results. On this

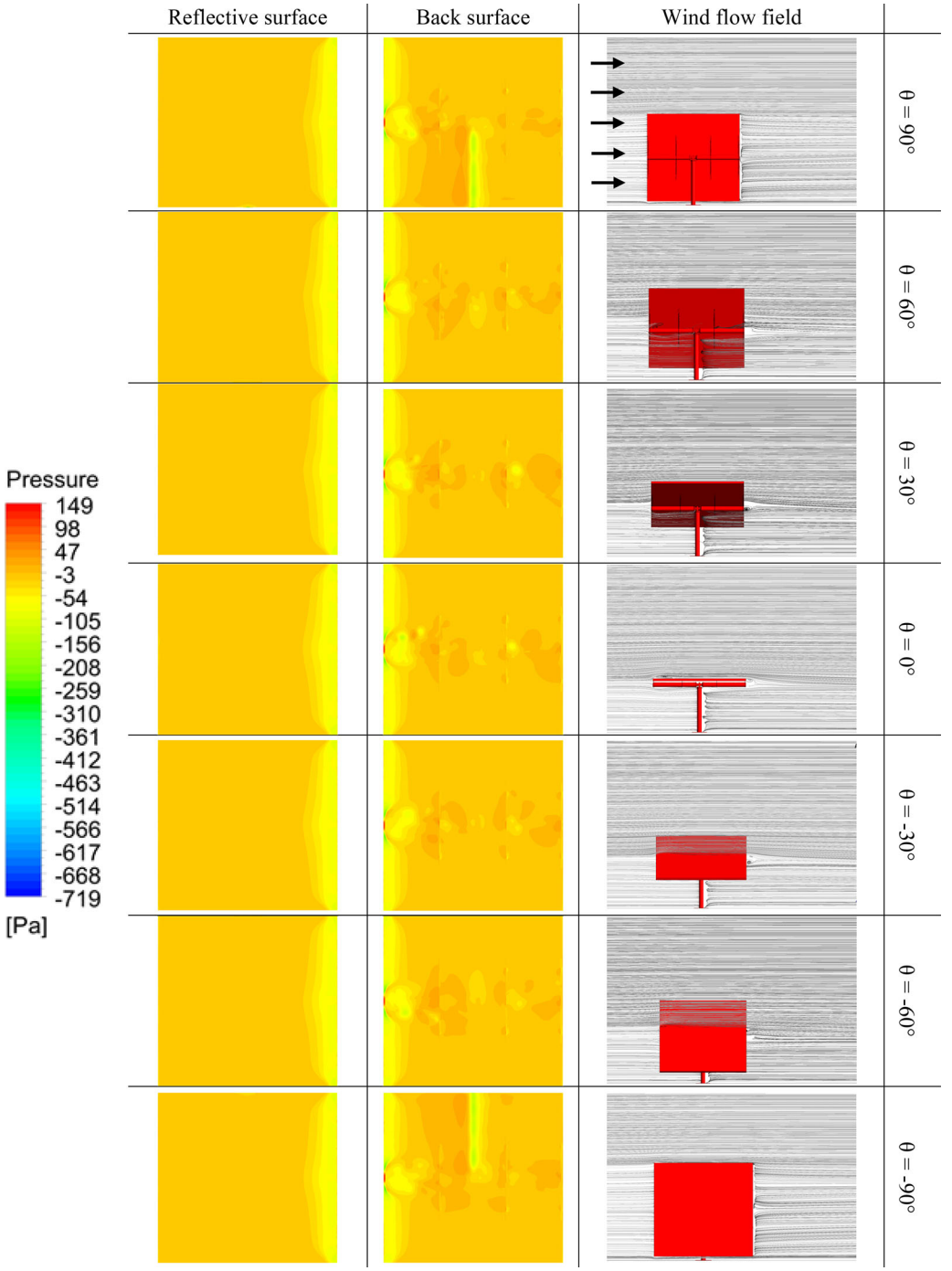

Figure 6. Pressure distribution on the heliostat at wind velocity of 15 m/s approaching at 90° incidence angle (β).

basis, and negligible difference between the two approaches, linear analysis was employed to reduce the computational cost of the analysis.

Furthermore, instead of developing a fully detailed multi-cell honeycomb core model, common practice, as used in this study, is to replace those cells with an equivalent three-dimensional orthotropic material model (has different material properties in three mutually perpendicular

directions). This approach has been effectively used in previous studies (Schwingshackl, Aglietti, and Cunningham 2006; Aydincak and Kayran 2009; Sorohan et al. 2016) due to the substantial advantages that can be obtained, which include delivering the same results as the fully detailed multi-cell honeycomb model, ease of modeling and model modification, reduced solution time, and fewer hardware resource requirements. In doing this, the honeycomb core's mechanical properties were calculated based on its geometrical properties (e.g., cell wall angle (φ), cell wall length (a) and cell wall thickness (t)) and material characteristics, using the relationships described by Nast (1997) and Gibson and Ashby (1997) (Appendix B). When designing a product using honeycomb cores, it is typical to select from the restricted variations of ready-made honeycomb. Therefore, it was assumed that the panel consists of a honeycomb core formed by regular hexagonal cells (cell wall angle of $\varphi = 30^\circ$). These are the most commonly used sandwich panel cores in industry applications, because they are easily manufactured and have good out-of-plane properties (Hu, You, and Yu 2013; Araújo et al. 2018). Moreover, and based on the preliminary analysis mentioned earlier to determine an initial structural configuration that provides a sensible tradeoff between structural integrity and weight reduction, the length and thickness of the honeycomb cell wall were selected to be $a = 6$ mm and $t = 0.03$ mm, respectively, which fall within the range of commercially available honeycomb cell sizes (Hexcel 1999; Yamashita and Gotoh 2005; Nayak 2012).

3. Results and discussion

3.1. Wind pressure distribution characteristics

Evaluating the structural responses of the honeycomb sandwich composite-based heliostat requires an understanding of the pressure loads acting on the surfaces of the panel due to wind forces. Therefore, having set up the numerical FSI model, the wind pressure distribution characteristics on the heliostat's sandwich composite panel were explored in detail. Figures 4–6 show wind pressure distributions on the heliostat's reflective and back surfaces under a wind velocity of 15 m/s for 0°, 45°, and 90° wind incidence angles (β), respectively, and a range of tilt angles (θ).

When the flow approaches the heliostat at 0° incidence angle (Figure 4), the structure intercepts the air's horizontal movement when flow is perpendicular to the heliostat's mirror surface, i.e., 90° tilt angle. This causes the flow in the front of heliostat structure to move toward stagnation (zero wind velocity), resulting in high pressure values, as stated by Bernoulli's law (pressure has a largest value when the velocity of the fluid is zero), at the middle of a span-wise line, decreasing toward the edges. This is expected as the flow accelerates at the edges to maintain continuity; it creates low-pressure regions on the reflector's surface.

Taking the same wind incidence angle but progressively changing the tilt angle from $\theta = 90^\circ$ to $\theta = 30^\circ$ results in a shift in the high pressure region toward the lower edge of the reflector, causing the structure to experience large wind pressures at the mirror surface's lower edge.

For the 0° tilt angle (stow position) experiencing wind at the same incidence angle, the wind loading has no noticeable effect on the structure compared to the remaining angles of operation. This is because the area at the front side of the reflector directly facing the wind is very small, allowing the incoming flow to become uniform and attached to the heliostat's surface. However, what is noticeable is that from the windward side the reflector's back surface has greater wind pressures compared to the upper surface. This pressure difference results in large lift forces close to the windward edge. From the leeward side of the heliostat, the opposite occurs, and wind pressures are higher at the reflective surface than the back surface. This is due to the depression region formed within the torque tube and the reflector's back surface, causing high suctions to occur at the heliostat's leeward side.

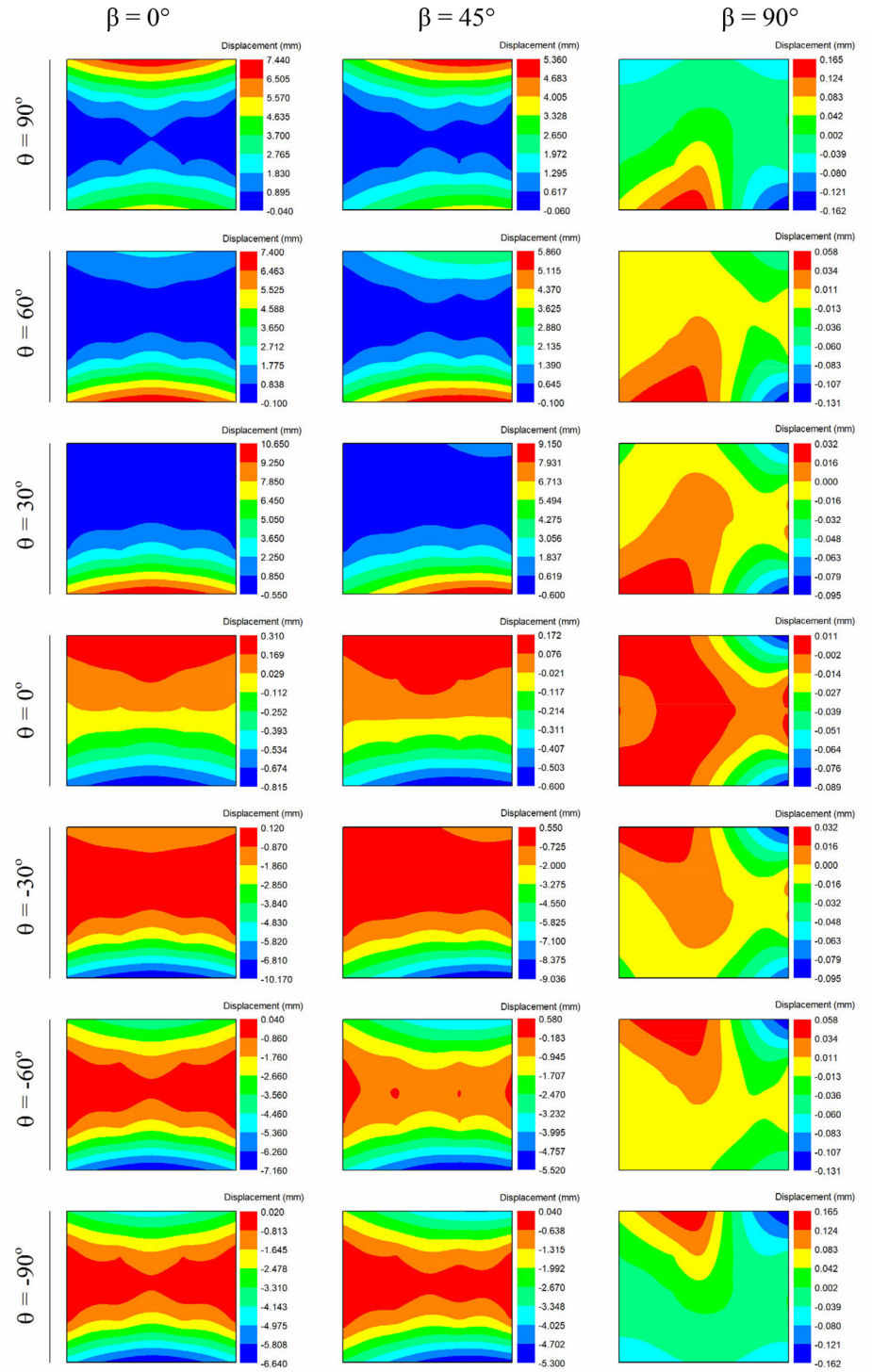

Figure 7. Displacement distribution of the heliostat surface at wind speed of 15 m/s for different tilt and wind incidence angles.

As the heliostat structure is moved from the stow position to a -90° tilt angle, the incoming wind at the same incidence angle acts on the back surface of the heliostat directly, resulting in high-pressure values at the middle of the heliostat's back surface.

Varying the wind incidence angle (β) from 0° to 45° for all tilt angles (Figure 5) causes the high-pressure regions located at the reflector's surface to shift toward the right edge. For all tilt angles excluding $\theta = 0^\circ$, a reduction in wind loading was observed compared to the same angles of operation when the flow approaches the heliostat at 0° incidence angle. This can be attributed to the fact that the heliostat's projected area directly facing the wind decreases with the increase in wind incidence angle, reducing the effect of the blockage and causing a decrease in the wind loading effect on the heliostat.

As the wind incidence angle gradually increases from $\beta = 45^\circ$ to $\beta = 90^\circ$ (Figure 6), the wind loading has no noticeable effect on the structure at this configuration for all given tilt angles. This is due to, as discussed in the stow position case, the area at the front side of the reflector directly facing the wind is very small, allowing the incoming flow to become uniform and attached to the heliostat's surface. In addition, the reflector's back surface on the windward side has greater wind pressures compared to the reflective surface. This pressure difference results in large lift forces close to the windward edge. However, what is noticeable from the pressure distributions on the heliostat's back surface at this configuration ($\beta = 90^\circ$) is that both the pedestal and torque tube have an influence on the pressure distributions at the back of the reflector. At tilt angles 90° and -90°, a depression region forms within the pedestal and the reflector, causing high suctions to occur at the heliostat's back surface. This depression region starts to demise as the heliostat structure moves toward the stow position ($\theta = 0^\circ$).

3.2. Heliostat structural behavior

Having discussed the wind pressure distributions on the heliostat surfaces at varying tilt and incidence angles, it was decided to evaluate the structural behavioral characteristics of the heliostat's sandwich composite panel under those wind-loaded conditions in great detail.

3.2.1. Deflections

The aerodynamic loads experienced by heliostats can lead to structural deformations that can markedly affect mirror quality (the sunlight is reflected with less accuracy). Therefore, the stiffness of the heliostat panel has a direct impact on overall plant efficiency. This section therefore analyses the heliostat panel deformations caused by wind loads under varying conditions.

Figure 7 presents the displacement distributions of the heliostat panel (calculated normal to the surface of the reflector) for different tilt angles at a wind velocity of 15 m/s approaching at 0°, 45°, and 90° wind incidence angles (β), respectively. Positive displacement values indicate that the deflection of the panel is inward to the plane (i.e., the surface of the reflector), and negative displacement values indicate that the deflection is outward to the plane of action. Since the study is focusing on understanding the structural behavior of the heliostat's composite structure, it was assumed that both the pedestal and torque tube are rigid enough to withstand these wind conditions. Therefore, both components were constrained to obtain only the heliostat's sandwich composite panel behavior.

Starting with the $\theta = 90^\circ$ tilt angle operational condition experiencing wind at $\beta = 0^\circ$ incidence angle (Figure 7), the areas with maximum displacement values are located at the heliostat's lower and upper edge regions, with higher displacement values located at the upper edge. These two regions are not fully supported by the steel attachments and majorly rely on the sandwich panel's stiffness to provide the reflective mirror module with the necessary rigidity and support. At this tilt orientation, it was found that the sandwich panel deformation contributes around 63% of the

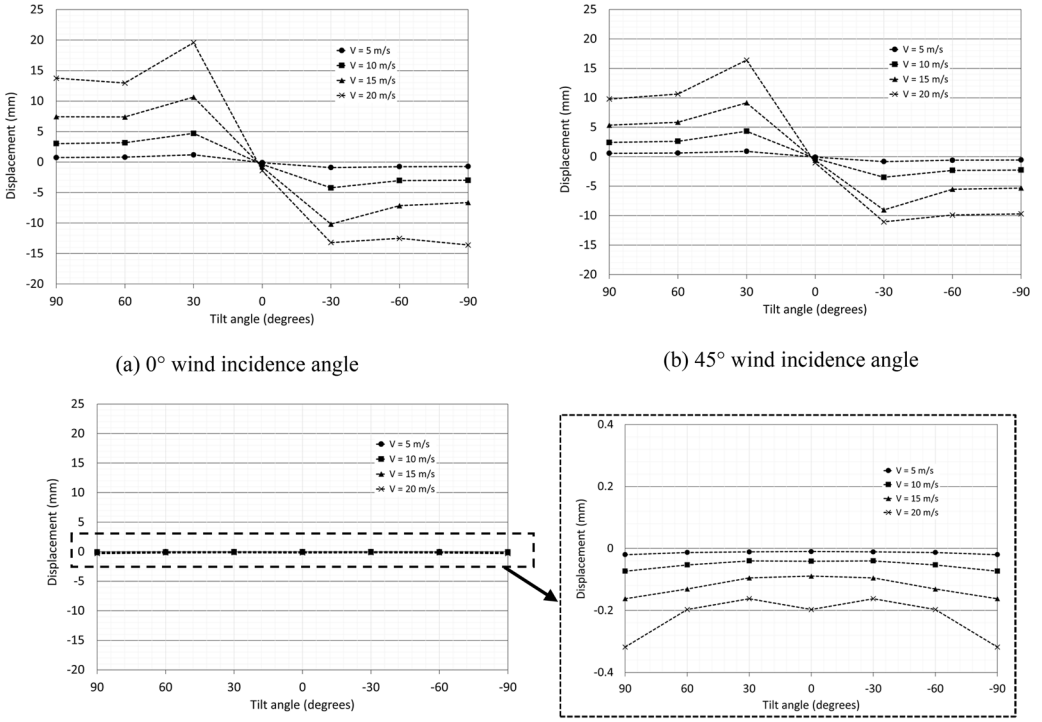

(a) 0° wind incidence angle

(b) 45° wind incidence angle

(c) 90° wind incidence angle

Figure 8. Wind velocity and tilt angle effects on the heliostat surface's maximum recorded displacement for 0°, 45° and 90° wind incidence angle.

total displacement experienced by the heliostat and the remaining 37% is handled by the supporting steel attachments. As the structure's tilt angle gradually decreases from $\theta = 90^\circ$ to $\theta = 30^\circ$ for the same 0° wind incidence angle results, the structure experiences larger displacement values at the reflector surface's lower edge, due to the progressive shift in the high-pressure regions toward the heliostat's lower edge as the tilt angle varies from 90° to 30°. This increase in displacement with the decrease in tilt angle triggers the supporting steel attachments to act upon the pressure concentration at the lower edge to preserve the deformations of the heliostat, causing the contribution of the attachments to increase to about 42%.

Taking the same wind incidence angle but changing the tilt angle from $\theta = 30^\circ$ to $\theta = 0^\circ$, the recorded maximum displacement values significantly decrease, due to the small windward facing area causing a significant reduction in the wind load on the heliostat structure and consequently reduces the contribution of the steel attachments to the total deformation to about 36%. Having said that, the resultant lift forces close to the panel's windward edge and the high suctions that occur at the leeward edge's side cause its windward and leeward edges to deform in the upward and downward directions respectively.

When the structure's tilt angle alters from the stow position to a -90° tilt angle (heliostat's back surface facing the wind) at the same incidence angle ($\beta = 0^\circ$), it is interesting to note that the maximum displacement values were slightly lower than those recorded when the flow is acting on the mirror surface, i.e., $\theta = 90^\circ$ to $\theta = 30^\circ$. This is due to the influence of the heliostat's supporting components (pedestal, torque tube, steel attachments) on the incoming flow, causing a shielding effect.

The progressive shift in the high-pressure regions, observed in the flow modeling, toward the right edge as the incidence angle vary from 0° to 45° led to the same behavior being observed in

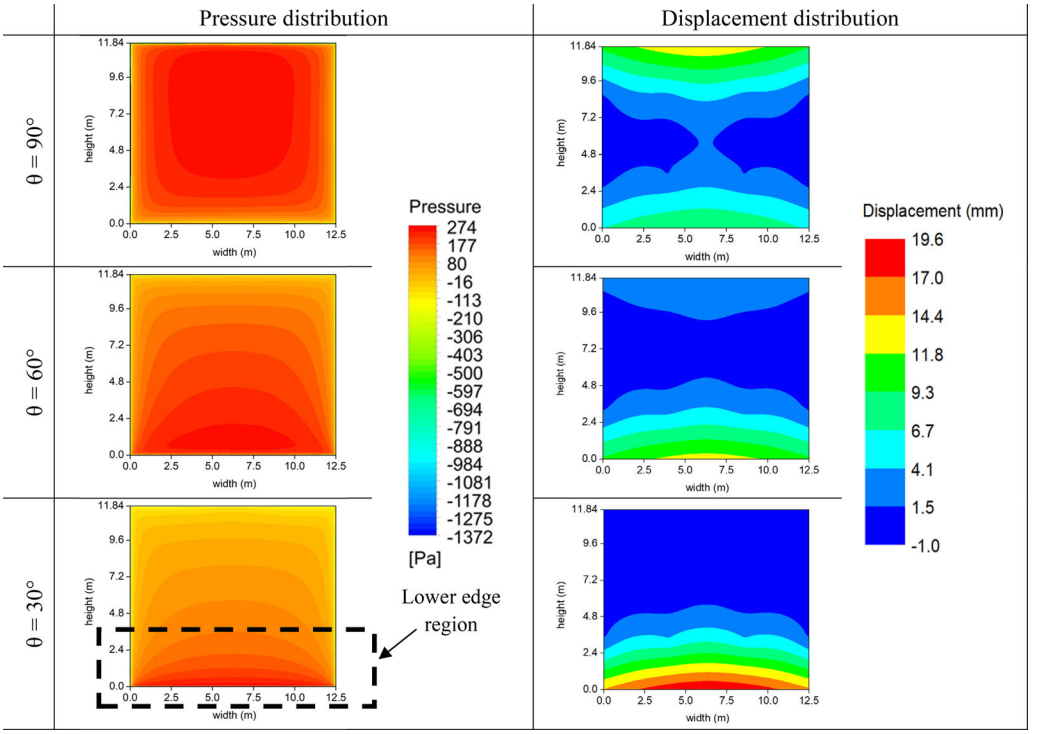

Figure 9. Pressure and displacement distribution of the heliostat surface for 90°, 60° and 30° tilt angles (θ) at wind velocity of 20 m/s approaching at 0° incidence angle (β).

the maximum-recorded displacement regions (Figure 7), but with lower displacement values than the 0° incidence angle operational condition for all tilt angles, due to a reduced pressure gradient between the heliostat's reflective and back surfaces as the wind incidence angle changes from $\beta = 0°$ to $\beta = 45°$. The same trend was observed in the supporting steel attachments' deformation contribution as the tilt angle alters from vertical to horizontal. The identified decrease in wind pressure imposed upon the panel was reflected in the contribution of the supporting steel attachments to the total displacement experienced by the heliostat; the deformation percentage values were lower than those recorded when flow approaches the heliostat at 0° incidence angle. The same shielding effect has been noticed at this configuration, and the maximum displacement values recorded with the back of the heliostat facing the wind were slightly lower than those recorded when the flow is acting on the mirror surface, i.e., $\theta = 90°$ to $\theta = 30°$.

The maximum displacement values significantly decreased as the wind incidence angle increased to $\beta = 90°$ for all tilt angles (Figure 7), because of the very small area at the front of the reflector directly facing the wind that allows incoming flow to become uniform and attached to the heliostat's surface, causing a significant reduction in the wind loading effect on the heliostat. At this configuration ($\beta = 90°$), the resultant lift forces close to the panel's windward edge and the high suctions that occur on the leeward edge causes the windward and leeward edges to deform in the upward and downward directions respectively. However, the displacement distribution is not the same for all tilt angles. At tilt angles 90°and $-90°$, the areas with maximum displacement values are located at the heliostat's lower and upper edge regions respectively, due to the depression region that forms within the pedestal and the reflector. This region starts to reduce in size as the heliostat structure moves toward the stow position from $\theta = \pm 90°$, and the displacement distribution tends to become symmetric about the torque tube axis.

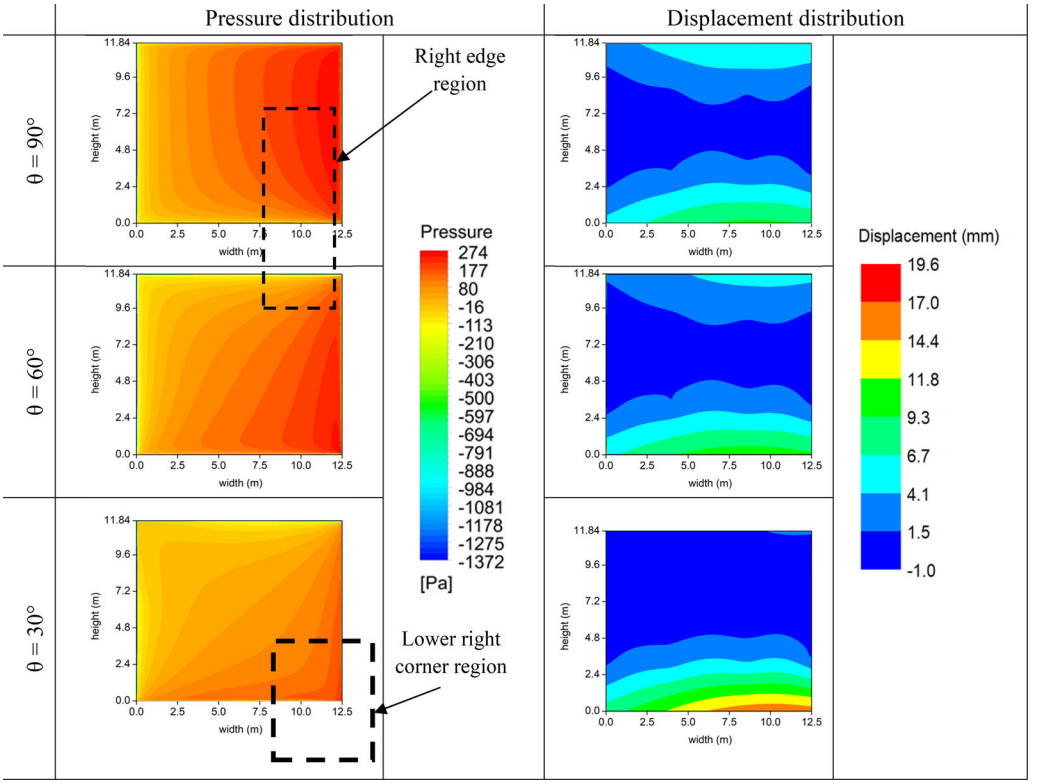

Figure 10. Pressure and displacement distribution of the heliostat surface for 90°, 60° and 30° tilt angles (θ) at wind velocity of 20 m/s approaching at 45° incidence angle (β).

Having discussed the displacement distribution of the heliostat's sandwich composite panel for the 15 m/s case, the influence of varying wind velocity on the heliostat surface's maximum resultant displacement at varying tilt and incidence angles is illustrated in Figure 8.

For 0° wind incidence angle (Figure 8a), the trends in maximum resultant displacement at the sandwich composite panel are almost similar for the four wind velocity cases, except for the stow position ($\theta = 0°$). The effect of wind velocity on the structural deformation of the heliostat panel when $\theta = 0°$ was negligible. This is because of flow uniformity (the projected area of the reflector directly facing the wind is at its minimum), which causes a significant decrease in the wind loading effect on the panel at this tilt orientation for all wind velocities (5–20 m/s). At a wind velocity of 5 m/s, there is a relatively small difference in the sandwich panel's maximum recorded displacement at different tilt angles. This implies that the heliostat orientation has no significant effect on the recorded maximum deflections of the heliostat panel when subjected to a wind of 5 m/s. For higher wind velocities, greater than 10 m/s, this effect becomes more pronounced and the difference in the maximum displacement values at different tilt angles increases to a maximum at a wind velocity of 20 m/s. Comparing the negative tilt angles ($\theta = -30°$ to $\theta = -90°$) with the positive ones ($\theta = 90°$ to $\theta = 30°$), it can be seen that the maximum displacement values were slightly lower, because of the effect of the heliostat's supporting components (i.e., pedestal, torque tube, steel attachments) on the incoming wind, causing a shielding effect.

For the positive tilt angles, between $\theta = 90°$ (heliostat directly facing the air flow) and $\theta = 30°$, the aerodynamic loads imposed upon the heliostat at $\theta = 30°$ generate a more detrimental effect on the heliostat's sandwich composite panel than do the other tilt angles. Figure 9 shows the pressure and displacement distribution of the heliostat surface from 90° to 30° tilt angles for a wind velocity of 20 m/s approaching at 0° wind incidence angle. When the structure is tilted at

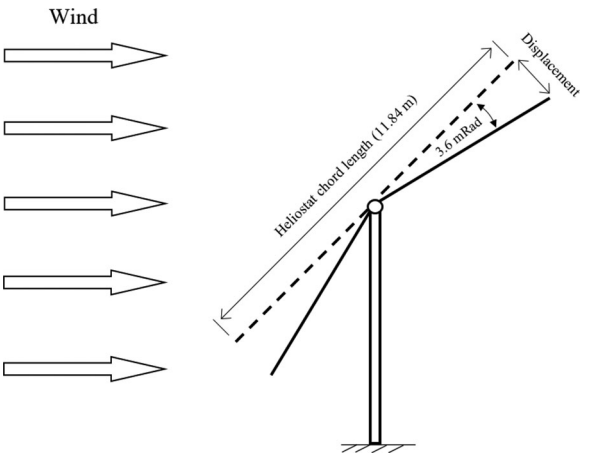

Figure 11. Interpretation of the reflective surface's maximum allowable deflection (Björkman 2014).

angles of 90° and 60°, the high wind pressure is distributed over a relatively large area of the heliostat's panel compared with the 30° tilt angle condition. However, with the case of 30° tilt angle, the wind directly strikes the panel's lower edge region. Because this region is not fully supported by the steel attachments and relies on the stiffness of the sandwich panels, the structure experiences larger displacements than in the 90° and 60° operational conditions.

As illustrated for the 0° wind incidence angle operational condition, the maximum displacement results for a wind incidence angle of $\beta = 45°$ (Figure 8b) revealed the same patterns of variation but with lower magnitudes than the $\beta = 0°$ condition illustrated earlier (Figure 8a). This is expected as discussed previously that the blockage to wind flow provided by the heliostat structure decreases with increasing wind incidence angle. This, in turn, causes a decrease in the aerodynamic loads imposed upon the heliostat panel, resulting in lower structural deflections. Similar to the case of 0° wind incidence angle, it can be clearly observed that the maximum displacement values for the negative tilt angles ($\theta = -30°$ to $\theta = -90°$) are lower than those observed for the positive tilt angles ($\theta = 90°$ to $\theta = 30°$) (Figure 8b), confirming the shielding effect of the heliostat's supporting components and torque tube on the incoming wind. From the results in Figure 8b, it is clear that the effect of heliostat's tilt orientation on the sandwich panel's maximum deflection becomes more vital as wind velocity increases above 10 m/s, particularly when the heliostat structure is tilted at an angle of $\theta = 30°$ and subjected to a wind of 20 m/s. Expanding on this, the pressure and displacement distribution of the heliostat surface from 90° to 30° tilt angles for a wind velocity of 20 m/s approaching at 45° incidence angle is shown in Figure 10. The high wind pressure is distributed along almost the entire right edge region of the panel when the structure is tilted at an angle of 90° and 60°. This region is supported by both the stiffness of the sandwich panel and also the steel attachment, explaining the lower structural deflections in comparison to the 30° tilt angle condition. As the heliostat structure is moved from $\theta = 60°$ to a 30° tilt angle, the incoming wind at the same incidence angle acts on the lower right corner region of the panel directly, resulting in higher wind pressures in that region. As a result, the panel's lower edge region is not fully supported by the steel attachments and relies heavily on the sandwich panel's stiffness, so the panel experiences larger displacement compared to 90° and 60° tilt angles.

The reduction in the maximum displacement results of the heliostat's sandwich composite panel caries on as the wind incidence angle gradually increases until it reaches $\beta = 90°$ for all tilt angles (Figure 8c). This significant drop in maximum displacement is due to flow uniformity causing a major reduction in the wind loading on the structure. This implies that the heliostat panel at 90° wind incidence angle, irrespective of tilt angle, is not affected by wind loadings at wind velocities of 20 m/s and below.

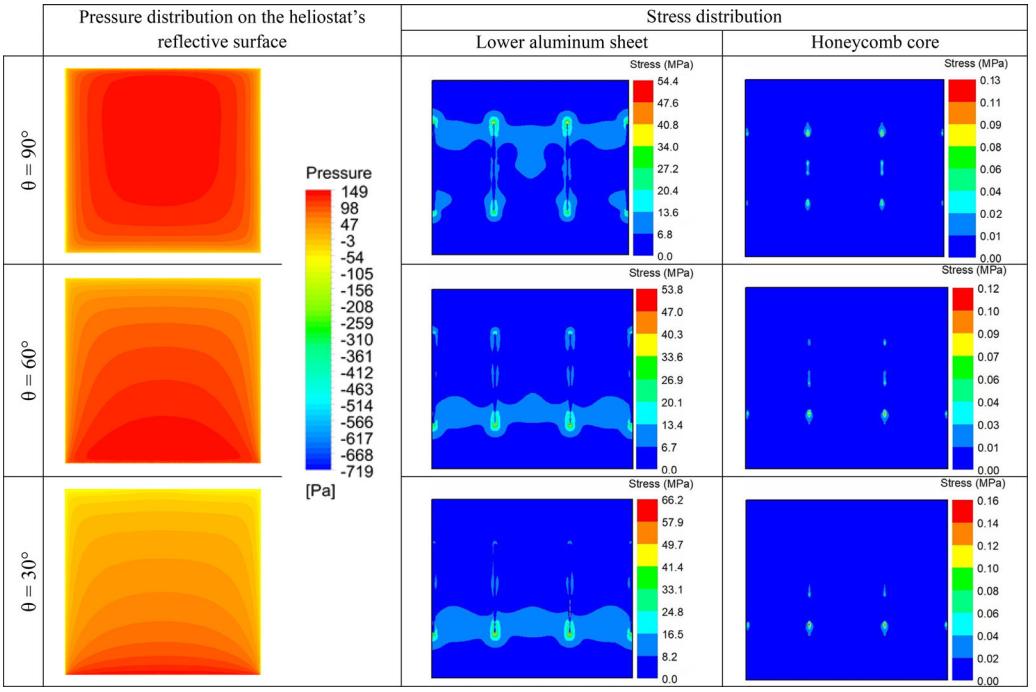

Figure 12. Pressure and stress distribution of the heliostat surface for 90°, 60°, 30° and 0° tilt angles (θ) at wind velocity of 15 m/s approaching at 0° incidence angle (β).

Compared to all of the other velocities explored, wind loadings at 20 m/s have the most substantial effects on the resultant displacement of the heliostat system for the operational conditions investigated. In all of the conditions studied, the largest resultant displacement is of 19.6 mm taking place at a tilt angle of 30° under the effect of wind approaching at 0° incidence angle. For reliable operation of a heliostat, it is required that its structure should be able to keep its deformation low enough that the acceptance angle loss of its reflective surface resides within tolerable limits. According to Kolb et al. (2007) and Strachan and Houser (1993), the Sandia requirements defined the maximum allowable reflective surface displacement angle caused by wind to be ±3.6 mRad. Björkman (2014) presented an approach, demonstrated in Figure 11, to evaluate the performance of the heliostat's reflective surface using the following triangular relationship (Eq. (1)) to calculate the maximum allowable displacement:

$$\tan(\pm 3.6\ mRad) = \frac{Displacement}{\frac{1}{2}(Heliostat\ \ chord\ \ length)} \tag{1}$$

In this study, to verify whether the proposed sandwich composite-based heliostat structure provides good optical performance, the same approach was used. Given that the heliostat's chord length is 11.84 m, the maximum allowable displacement was found to be approximately ±21.3 mm. On this basis, the deformation of the structure from the simulation suggests that it is within the allowable threshold and may be suitable for use as a heliostat.

3.2.2. Stress distributions

Having discussed the deflection of the heliostat's sandwich composite panel at varying operational conditions, it was decided to explore the stress distribution characteristics of the heliostat's sandwich composite panel under those conditions in detail, to better understand and evaluate the structural strength of the sandwich panel. By locating regions of high stress in the sandwich

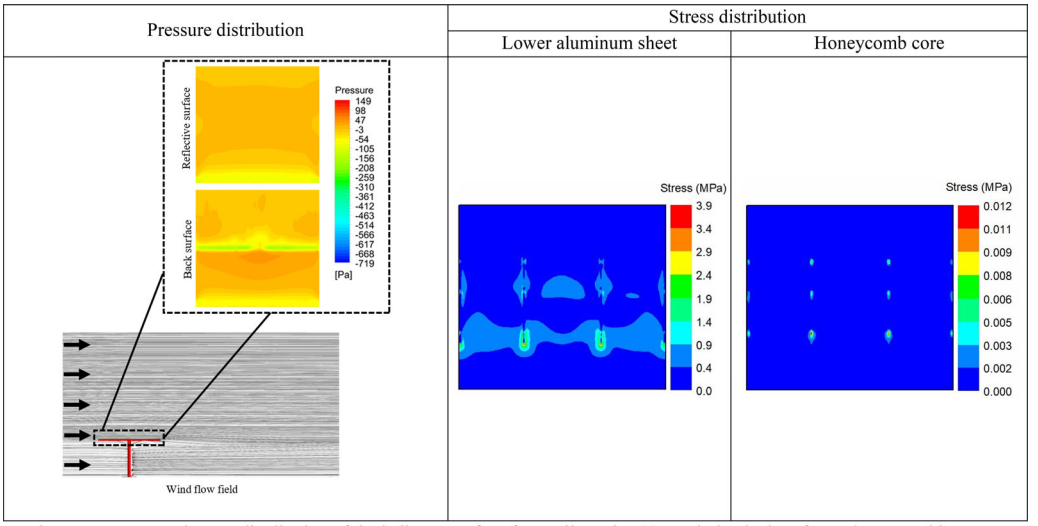

Figure 13. Pressure and stress distribution of the heliostat surface for 0° tilt angles (θ) at wind velocity of 15 m/s approaching at 0° incidence angle (β).

panel, it was found that the highly stressed regions are located at the junction between the sandwich panel and the supporting steel attachments. Consequently, the two components of the sandwich panel with the highest probability of experiencing material failure are the lower aluminum sheet and the aluminum honeycomb core. The study thus focused on evaluating the stress distribution characteristics of those two layers. Figures 12–17 show the stress distributions of the heliostat panel's lower aluminum sheet and the honeycomb core for different tilt angles (θ) at a wind velocity of 15 m/s approaching at 0°, 45°, and 90° incidence angles (β), respectively.

When flow is perpendicular to the heliostat's reflective surface, i.e., 90° tilt angle and 0° wind incidence angle (Figure 12), the high stress regions are located at the upper and lower ends of the interface between the steel attachments and the back surface of the panel, with higher stresses seen at the upper ends. The heliostat panel is subjected to a wind gradient (the wind strength increases with height above ground). This explains the higher stresses at the upper ends of the interface compared to the lower ends.

Taking the same wind incidence angle and decreasing the tilt angle from $\theta = 90°$ to $\theta = 30°$ (Figure 12), higher stress concentrations are located near the lower ends of the interface, corresponding to the progressive shift in the high-pressure regions at the mirror surface toward the lower edge as the structure's tilt angle (θ) moves from 90° to 30°. At this operational condition ($\theta = 30°$, $\beta = 0°$), the panel experiences the maximum stress, because at this orientation the heliostat experiences the maximum downward directed lift force due to the high pressure on its front side and low pressure and high velocities below the structure. The wind at this tilt orientation ($\theta = 30°$) strikes the panel's lower edge region directly. This region is predominantly dependant on the sandwich panel's stiffness only (not fully supported by the steel attachments) for delivering the necessary rigidity and support for the reflective mirror module. This, therefore, causes an increase in the structural deflection of the panel's lower edge region, resulting in higher stresses at the lower ends of the interface between the steel attachments and the panel's back surface.

For the same incidence angle ($\beta = 0°$), the recorded maximum stress values drop significantly when the heliostat's tilt angle decreases from $\theta = 30°$ to $\theta = 0°$ (Figure 13). This is because the projected area of the reflector directly facing the wind becomes very small, allowing uniformity of flow that significantly decreases the wind loading effect on the heliostat structure.

By altering the tilt angle gradually from $\theta = 0°$ to $\theta = -90°$ (Figure 14), such that the flow is from the backside of the structure, the heliostat's windward projected area increases, as does the

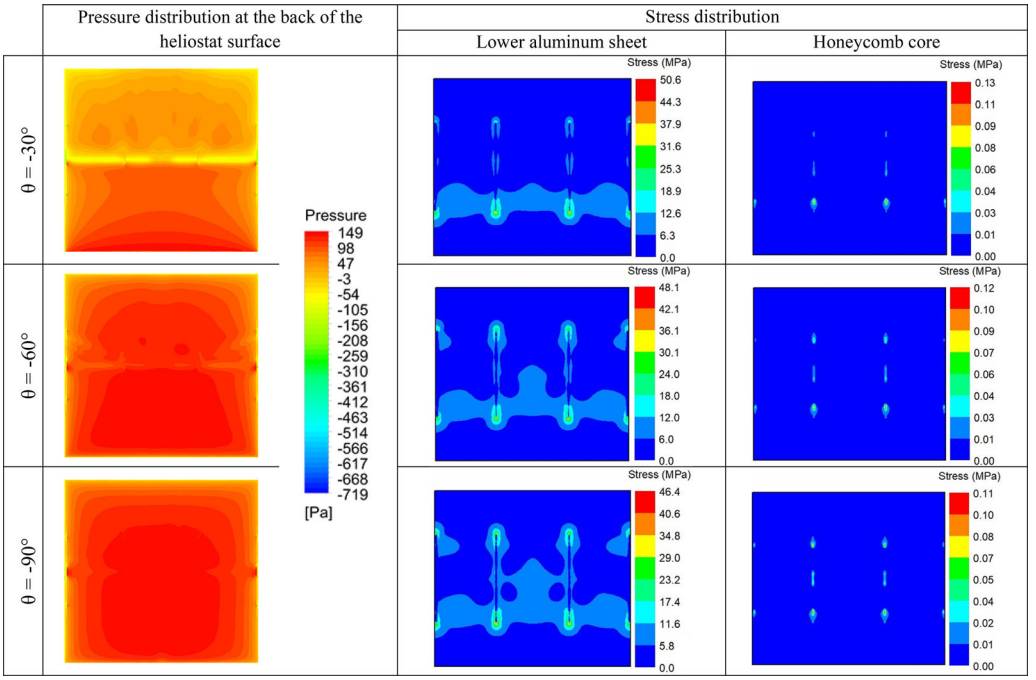

Figure 14. Pressure and stress distribution of the heliostat surface for −30°, −60° and −90° tilt angles (θ) at wind velocity of 15 m/s approaching at 0° incidence angle (β).

wind loading effect on the heliostat structure, causing an increase in stress at the ends of the interface between the steel attachments and the panel's back surface. However, with that being said, the recorded maximum stress values were lower in comparison with those recorded when the flow is acting on the heliostat's mirror surface, i.e., $\theta = 90°$ to $\theta = 30°$ (Figure 12), due to the shielding effect caused by the heliostat's supporting components.

The gradual variation in the wind incidence angle (β) from 0° to 45° for all tilt angles (Figure 15) causes the high-stress regions located at the interface between the steel attachments and the back surface of the panel to shift progressively toward the two attachments to the right. Furthermore, and as a result of the decrease in wind-induced forces caused by the reduction in the pressure gradient between the heliostat's reflective and back surfaces, the stress levels gradually decrease as the wind incidence angle changes from $\beta = 0°$ to $\beta = 45°$ (Figure 16). In addition, similar to the 0° wind incidence operational condition, the same shielding effect has been observed at this configuration ($\beta = 45°$) (Figures 15 and 16), and the maximum stress values recorded with the heliostat's back surface facing the wind ($\theta = -30°$ to $\theta = -90°$) were slightly lower than those recorded when the flow is acting on the heliostat's mirror surface ($\theta = 90°$ to $\theta = -30°$).

The reduction in stress values continues as the wind incidence increases from 45° to 90° (Figures 16 and 17), due to the significant decrease in the projected area of the heliostat directly facing the wind, permitting uniformity of flow that causes a significant drop in the wind loading effect on the structure. For tilt angles 90°and −90°, high stress regions are observed at the aluminum sheet's lower and upper edge regions respectively. This is because of the depression region that forms within the pedestal and the panel, which reduces as the structure moves toward the stow position from $\theta = \pm 90°$.

Having investigated the stress distribution of the heliostat's sandwich composite panel for the 15 m/s loading condition, the effect of changing wind velocity on the maximum stresses at the

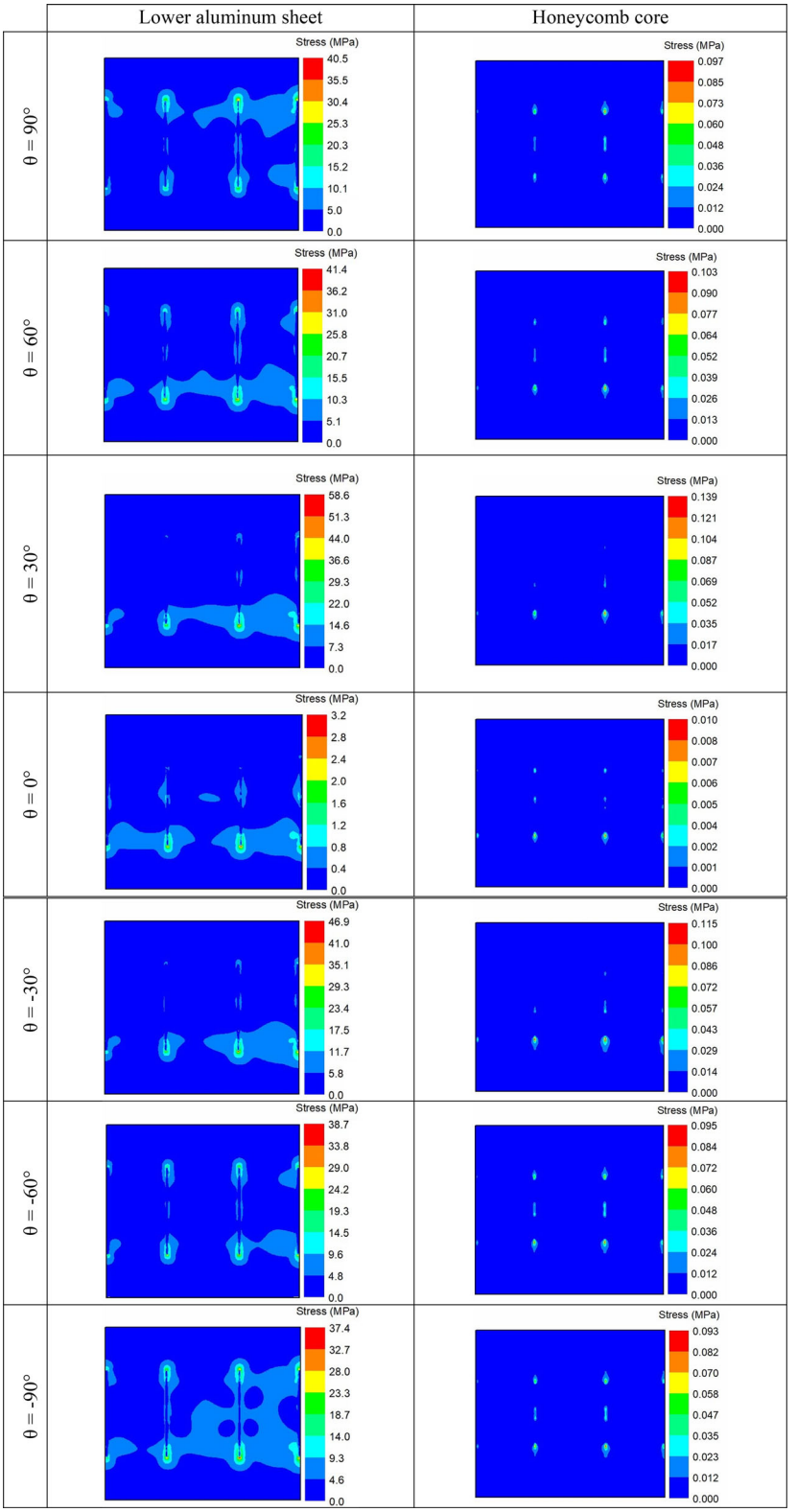

Figure 15. Stress distribution of the heliostat surface for different tilt angles at wind velocity of 15 m/s approaching at 45° incidence angle.

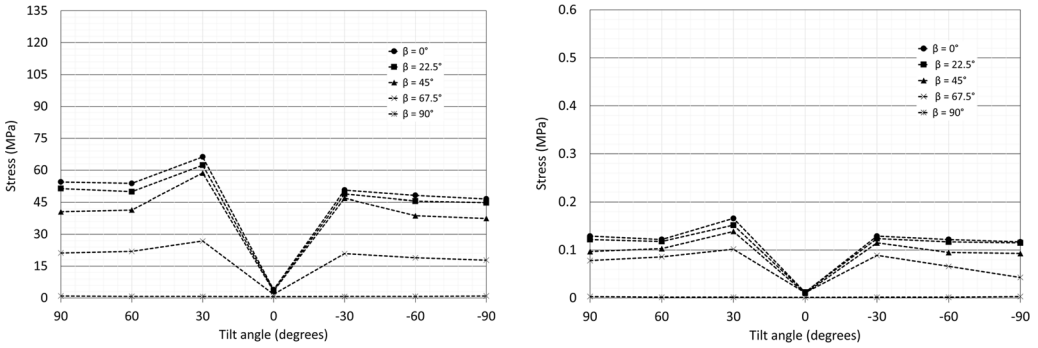

(a) Lower aluminum sheet (b) Honeycomb core

Figure 16. Wind incidence angle effect on the heliostat's maximum recorded stress for different tilt angles at wind velocity of 15 m/s.

heliostat panel's lower aluminum sheet and honeycomb core for different tilt and incidence angles is shown in Figures 18–22.

Starting with the 0° wind incidence angle results (Figure 18), increasing wind velocity affects the recorded maximum stress values at both the lower aluminum sheet and the honeycomb core by increasing their magnitude, although at different rates. Because of the decrease in the wind loading effect on the panel at this tilt orientation, the effect of increased wind velocity on the maximum stress values recorded at the panel's lower aluminum sheet and honeycomb core for the case of $\theta = 0°$ is insignificant.

As wind velocity increases above 10 m/s, the effect of heliostat's tilt orientation on the maximum stresses at both the lower aluminum sheet and the aluminum honeycomb core becomes more noticeable, and the variance in the maximum stress values at different tilt angles escalates to a maximum when wind strikes the heliostat panel with a velocity of 20 m/s. With the gradual increase in wind velocity, the shielding effect caused by the heliostat's supporting components becomes more pronounced, and the maximum stress values recorded for the negative tilt angles ($\theta = -30°$ to $\theta = -90°$) were lower than those observed for the positive tilt angles ($\theta = 90°$ to $\theta = 30°$) (Figure 18).

As shown in Figure 18, wind loadings with a velocity of 20 m/s striking the heliostat structure at $\theta = 30°$ tilt angle cause more harmful effects on the sandwich panel than any other tilt angle. Expanding on this, Figure 19 illustrates both pressure and stress distribution results for a wind velocity of 20 m/s approaching at 0° wind incidence angle. Unlike the 90° and 60° tilt angle conditions, where the loads are distributed over a large area of the heliostat's panel, the high wind pressure at the 30° tilt angle operational condition is concentrated in a particular region; the panel's lower edge region. Because of this, and given that this region is dependent upon the sandwich panel's stiffness only, the panel experiences larger deflections at the lower edge region. This high bending due to wind loads, in addition to the strong wind pressure imposed upon that region, induces higher stresses than do the other tilt angles, at the lower ends of the interface between the steel attachments and the panel's back surface.

The recorded maximum stress values when the flow approaches the heliostat at a 45° incidence angle (Figure 20) show similar but lower variation patterns to the 0° wind incidence angle. This reduction corresponds to the decrease in the wind loading effect on the heliostat that occurs as a result of the reduced blockage effect (the heliostat's projected area directly facing the wind decreases with the increase in wind incidence angle), resulting in lower stresses in comparison to the $\beta = 0°$ operational condition in Figure 18. At $\beta = 45°$ (Figure 20), the same shielding effect caused by the heliostat's supporting components can be noticed when comparing the negative tilt

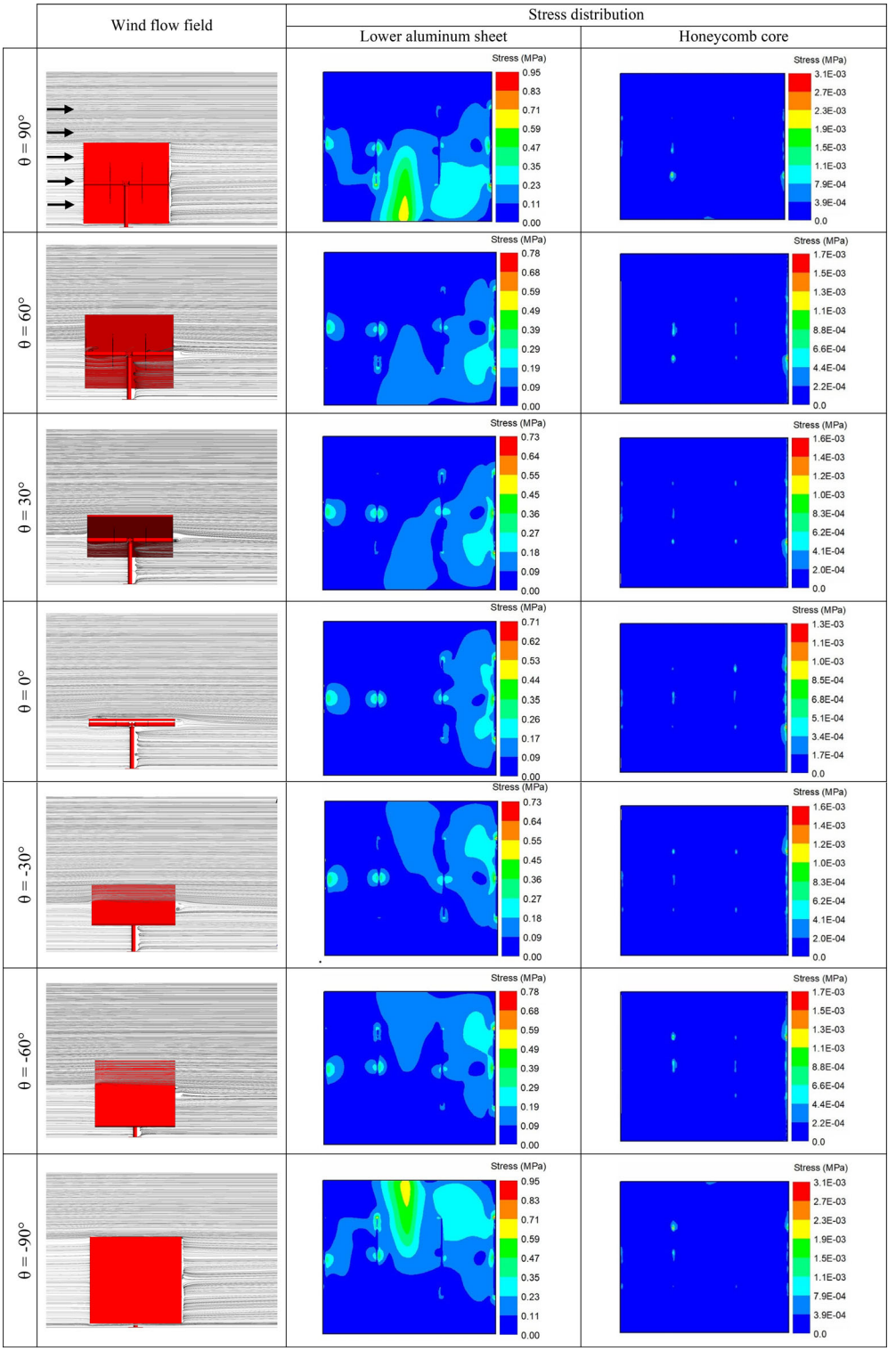

Figure 17. Stress distribution of the heliostat surface for different tilt angles at wind velocity of 15 m/s approaching at 90° incidence angle (β).

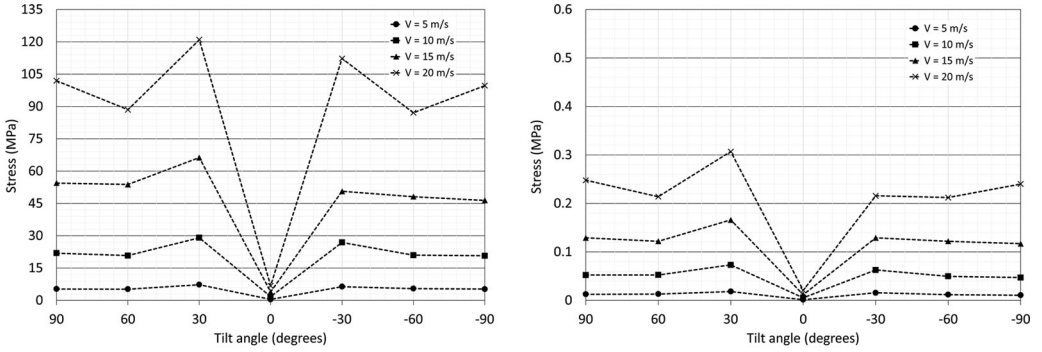

(a) Lower aluminum sheet (b) Honeycomb core

Figure 18. Wind velocity and tilt angle effects on the heliostat's maximum recorded stress for 0° wind incidence angle.

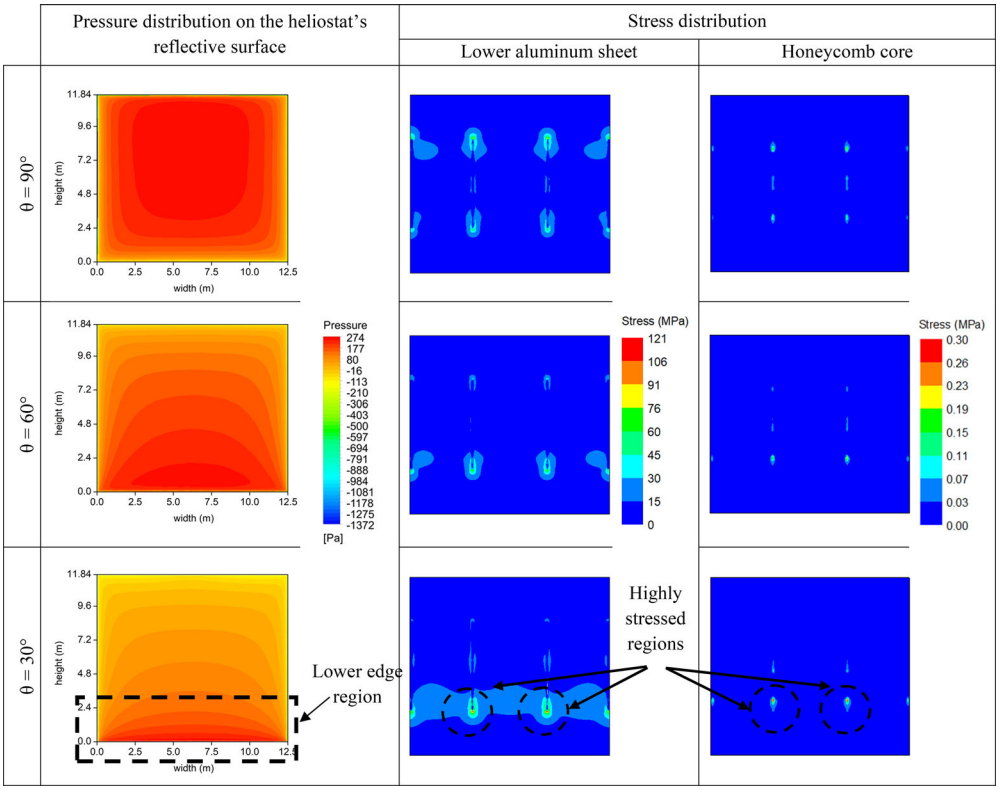

Figure 19. Pressure and stress distribution results for 90°, 60°, 30° and 0° tilt angles (θ) at wind velocity of 20 m/s approaching at 0° incidence angle (β).

angles ($\theta = -30°$ to $\theta = -90°$) with the positive ones ($\theta = 90°$ to $\theta = 30°$). This effect develops more strongly at higher wind velocities (greater than 10 m/s).

The heliostat at this wind incidence angle ($\beta = 45°$) experiences the maximum stress intensity when the panel is subjected to a wind of 20 m/s and tilted at an angle of 30°. Going into detail about this, the pressure and stress distribution results for a wind velocity of 20 m/s approaching at 45° wind incidence angle are presented in Figure 21. For the 30° tilt angle operational condition, the high wind pressure is concentrated over a smaller area (the lower right corner region of the panel) relative to the 90° and 60° tilt angle operational conditions, which puts direct pressure

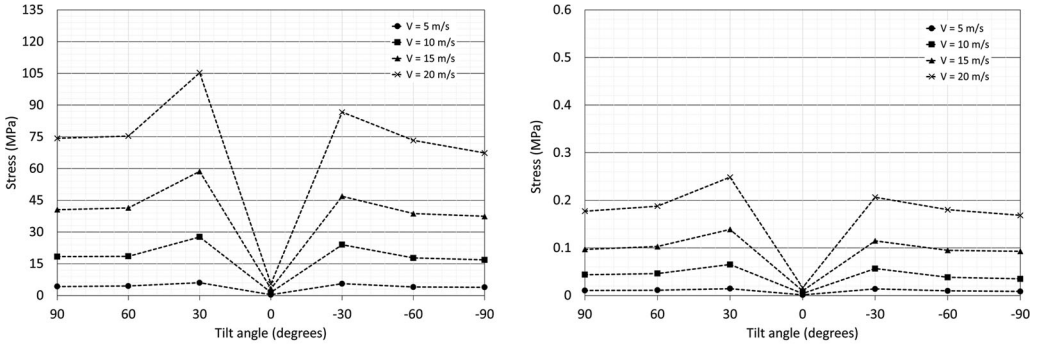

(a) Lower aluminum sheet (b) Honeycomb core

Figure 20. Wind velocity and tilt angle effects on the heliostat's maximum recorded stress for 45° wind incidence angle.

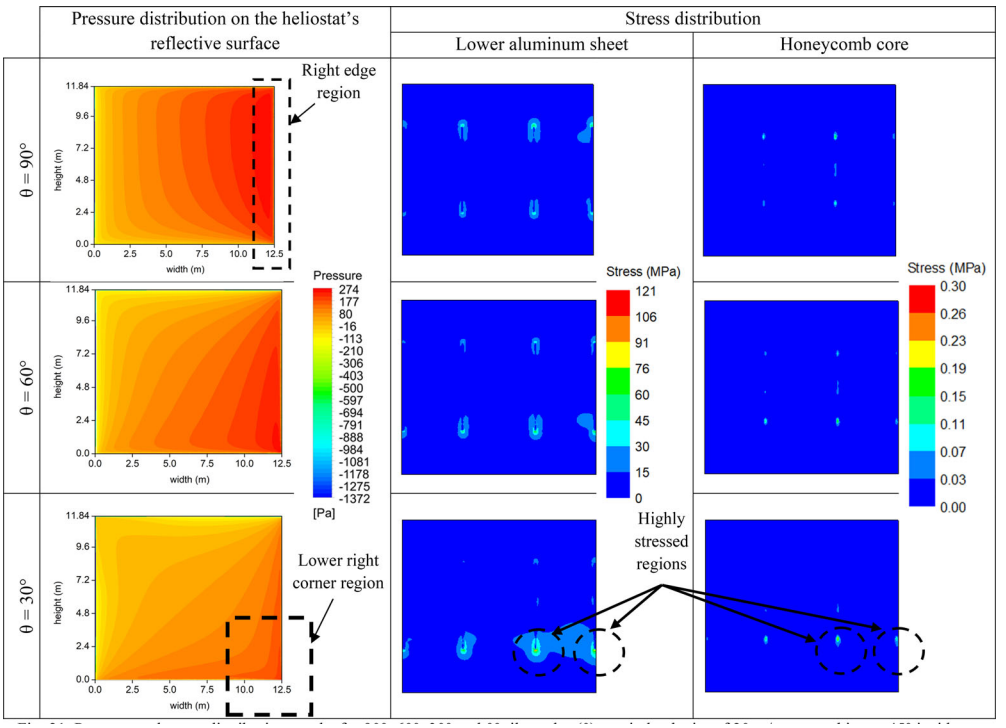

Figure 21. Pressure and stress distribution results for 90°, 60°, 30° and 0° tilt angles (θ) at wind velocity of 20 m/s approaching at 45° incidence angle (β).

on the regions at the junction between the sandwich panel and the two supporting steel attachments to the right. This causes the stresses to escalate and concentrate at the lower right ends of the interface between the steel attachments and the panel's back surface.

As the wind incidence angle increases from 45° to 90° for all tilt angles (Figure 22), its influence on the stress values increases and the values decrease to a minimum at $\beta = 90°$. This is because of the uniformity of flow that causes a significant decrease in the wind loading effect on the heliostat panel. This suggests that the heliostat panel's lower aluminum sheet and honeycomb core at a 90° wind incidence angle, regardless of any tilt angle, are not significantly influenced by wind loadings at wind velocities of 20 m/s and below.

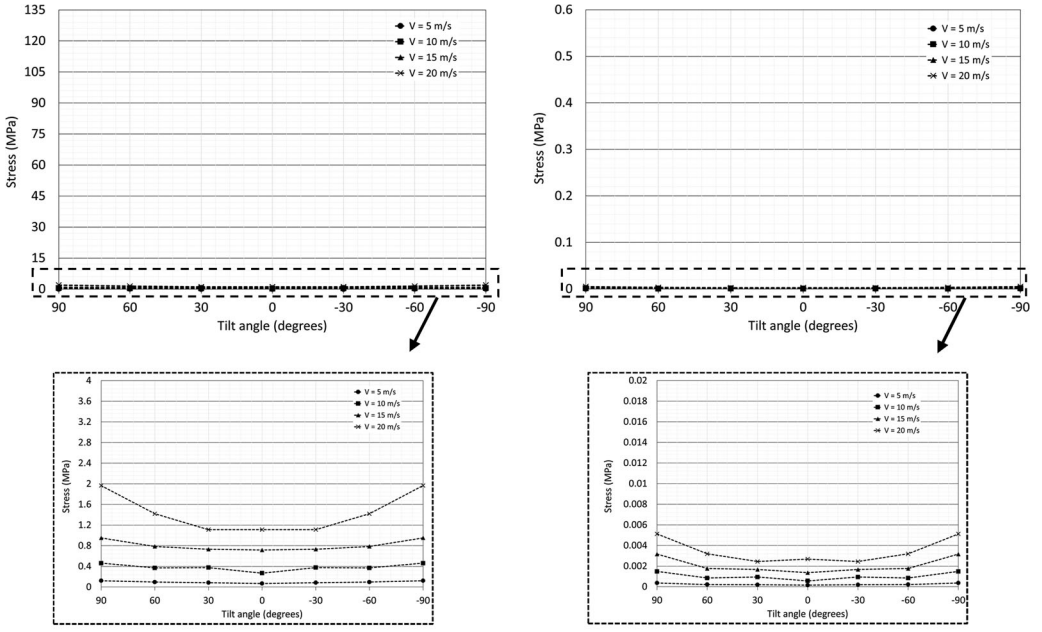

(a) Lower aluminum sheet

(b) Honeycomb core

Figure 22. Wind velocity and tilt angle effects on the heliostat's maximum recorded stress for 90° wind incidence angle.

Similarly, corresponding to the maximum resultant deformation of the structure, the worst case was found to be at a tilt angle of 30° with a wind flow at 0° to the heliostat surface and a velocity of 20 m/, producing calculated maximum stresses at both the lower aluminum sheet and the aluminum honeycomb core of 121.62 MPa and 0.307 MPa, respectively. The stresses imposed upon the panel can cause two of the most common forms of failure for honeycomb sandwich panels: face yielding and core crushing (Figure 23). Face yielding is the plastic collapse of the metal face sheet when the stress exceeds the yield strength of the material (Totten, Tiryakioglu, and Kessler 2018). Core crushing, on the other hand, is a core failure mode that is caused by cell-wall collapse due to cell-wall buckling when the flexure-induced compressive loading exerted upon the core exceeds the critical collapse strength of the core (Staal et al. 2009; Haghpanah et al. 2014).

According to Gibson and Ashby (Gibson and Ashby 1997), the critical collapse strength of honeycombs ($\sigma_{collapse}$) can be estimated using the following relationship (Eq. (2)):

$$\sigma_{\text{collapse}} = \frac{3\,\text{t}}{2\,\text{a}\cos\varphi\,(1+\sin\varphi)}\,\sigma_{\text{y}} \tag{2}$$

where φ is the cell wall angle, a is the cell wall length, t is the cell wall thickness and σ_{y} is the yield strength of the honeycomb's solid material. Given that σ_{y} for aluminum is 280 MPa, the core's critical collapse strength was found to be approximately 1.62 MPa. On this basis, the simulation suggests that the maximum stresses at both the lower aluminum sheet and the aluminum honeycomb core are within the permissible limits. This indicates that the heliostat's composite structure, with an achieved weight reduction of approximately 20% compared to the existing 148 m^2 steel-based ATS heliostat (Kolb et al. 2007), is unlikely to experience material failure and should maintain a very high optical performance when subjected to winds of 20 m/s and below. Based on these observations, it can be concluded that honeycomb sandwich composites are highly suitable for use as a heliostat mirror support structure.

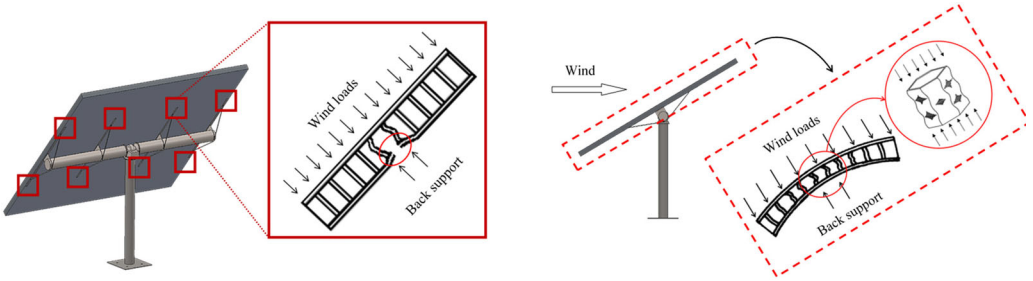

(a) Face yielding (b) Core crushing

Figure 23. Common failure forms of honeycomb sandwich panels (reproduced from Gibson and Ashby 1997 and Galletti, Vinquist, and Es-Said 2008).

4. Conclusion

This study investigated the use of honeycomb sandwich composites to develop a rigid, lightweight heliostat mirror support structure with the capability to endure the aerodynamic loads imposed upon them during operation. Numerical fluid-structure interaction (FSI) study was performed for several loading conditions with various tilt and wind incidence angles, to examine the structural behavior characteristics of the sandwich composite panel. The structural responses showed markedly different behavior characteristics under different operational conditions. From the results, it was shown that the effect of the heliostat's tilt orientation on the sandwich panel's maximum deflection and stresses becomes more pronounced as wind velocity increases above 10 m/s. This effect becomes more vital and the difference in the maximum displacement and stress values at different tilt angles escalated to a maximum at a wind velocity of 20 m/s. The study also showed that increasing wind incidence angle affected the recorded maximum displacement and stress results by reducing their magnitudes at different rates. When wind struck the heliostat structure at 0° and 45° incidence angles, the shielding effect caused by the supporting components and torque tube was clearly noticeable when the incoming wind acted on the reflector's back surface, and the maximum displacement and stress values were slightly lower compared to those recorded when the flow acted on the heliostat's mirror surface. From the operational conditions studied, it was concluded that the worst case was found to be at a tilt angle of 30° under the effect of wind flow at 0° to the heliostat surface with a velocity of 20 m/s. Despite this observation, it was found that the heliostat managed to maintain its structural integrity according to relevant optical and material failure standards, proving the potential of honeycomb sandwich composites in developing a stiff lightweight heliostat support structure that can withstand wind loads.

Conflicts of interest

The authors declare that there is no conflict of interest regarding the publication of this article.

ORCID

Sulaiman O. Fadlallah http://orcid.org/0000-0002-9654-2343
Timothy N. Anderson http://orcid.org/0000-0002-0972-5206

References

Aldaz, L., M. Burisch, F. Zaversky, M. Sánchez, C. Villasante, and D. Olasolo. 2018. Heliostat structural optimization: A study of wind load effects with CFD-FEM methods. *AIP Conference Proceedings* 2033 (1):210001.

Alijani, F., and M. Amabili. 2013. Nonlinear vibrations of laminated and sandwich rectangular plates with free edges. Part 1: Theory and numerical simulations. *Composite Structures* 105:422–36. doi:10.1016/j.compstruct.2013.05.034.

Alijani, F., M. Amabili, G. Ferrari, and V. D'Alessandro. 2013. Nonlinear vibrations of laminated and sandwich rectangular plates with free edges. Part 2: Experiments & comparisons. *Composite Structures* 105:437–45. doi:10.1016/j.compstruct.2013.05.020.

Araújo, H., M. Leite, A. R. Ribeiro, A. M. Deus, L. Reis, and M. F. Vaz. 2018. The effect of geometry on the flexural properties of cellular core structures. *Proceedings of the Institution of Mechanical Engineers, Part L: Journal of Materials: Design and Applications* 233 (3):146442071880551–347. doi:10.1177/1464420718805511.

Aydincak, İ., and A. Kayran. 2009. An approach for the evaluation of effective elastic properties of honeycomb cores by finite element analysis of sandwich panels. *Journal of Sandwich Structures & Materials* 11 (5):385–408. doi:10.1177/1099636209102891.

Ayub, M. Y., Z. Ahmer, S. R. Khan, and M. A. Shah. 2011. Mechanical behavior characterization of aluminum based honey comb structure by optimized modeling and numerical simulations. *Journal of Space Technology* 1 (1):26–33.

Balaji, G., and K. Annamalai. 2019. Numerical investigation of honeycomb filled crash box for the effect of honeycomb's physical parameters on crashworthiness constants. *International Journal of Crashworthiness* 24 (2): 184–98. doi:10.1080/13588265.2018.1424298.

Baumgart, C., T. Halle, C. Weigelt, L. Krüger, and C. G. Aneziris. 2018. Effect of honeycomb cell geometry on compressive properties: Finite element analysis and experimental verification. *Science and Technology of Materials* 30 (1):35–42. doi:10.1016/j.stmat.2018.02.001.

Behar, O., A. Khellaf, and K. Mohammedi. 2013. A review of studies on central receiver solar thermal power plants. *Renewable and Sustainable Energy Reviews* 23:12–39. doi:10.1016/j.rser.2013.02.017.

Bendjebbas, H., A. Abdellah-ElHadj, and M. Abbas. 2016. Full-scale, wind tunnel and CFD analysis methods of wind loads on heliostats: A review. *Renewable and Sustainable Energy Reviews* 54:452–72. doi:10.1016/j.rser.2015.10.031.

Birman, V., and G. A. Kardomateas. 2018. Review of current trends in research and applications of sandwich structures. *Composites Part B: Engineering* 142:221–40. doi:10.1016/j.compositesb.2018.01.027.

Björkman, N. 2014. Heliostat design. Master thesis, Department of Industrial Engineering and Management, KTH Royal Institute of Technology, Stockholm, Sweden.

Castellon, J. 2012. Cellular ceramics: Reinforced brick construction in the digital age. *Interceram* 61 (5):277–82.

Cheng, S., P. Qiao, and F. Chen. 2016. Numerical analysis of I-Lam honeycomb sandwich panels for collision protection of reinforced concrete beams. *Journal of Sandwich Structures and Materials* 1:1–26.

Çınar, O. 2014. Evaluation of effective elastic properties of honeycomb sandwich structures by optimization involving modal behavior. Master's thesis, Middle East Technical University, Turkey.

Diver, R. B., and J. W. Grossman. 1998. Sandwich construction solar structural facets. Report Number SAND98-2845C. Sandia National Laboratories, Albuquerque, NM.

Emes, M. J., M. Arjomandi, F. Ghanadi, and R. M. Kelso. 2017. Effect of turbulence characteristics in the atmospheric surface layer on the peak wind loads on heliostats in stow position. *Solar Energy* 157:284–97. doi:10.1016/j.solener.2017.08.031.

Fadlallah, S. O., T. Anderson, and R. Nates. 2021. Flow behaviour and aerodynamic loading on a stand-alone heliostat: Wind incidence effect. *Arabian Journal for Science and Engineering* 46 (8):7303–19. doi:10.1007/s13369-021-05405-0.

Galletti, G. G., C. Vinquist, and O. S. Es-Said. 2008. Theoretical design and analysis of a honeycomb panel sandwich structure loaded in pure bending. *Engineering Failure Analysis* 15 (5):555–62. doi:10.1016/j.engfailanal.2007.04.004.

Gibson, L. J., and M. F. Ashby. 1997. *Cellular solids: Structure and properties*. 2nd ed. Cambridge, UK: Cambridge University Press.

Goswami, D. Y. 2015. *Principles of solar engineering*. 3rd ed. New York, NY: CRC Press.

Haghpanah, B., J. Papadopoulos, D. Mousanezhad, H. Nayeb-Hashemi, and A. Vaziri. 2014. Buckling of regular, chiral and hierarchical honeycombs under a general macroscopic stress state. *Proceedings. Mathematical, Physical, and Engineering Sciences* 470 (2167):20130856. doi:10.1098/rspa.2013.0856.

Heimbs, S., D. Vogt, R. Hartnack, J. Schlattmann, and M. Maier. 2008. Numerical simulation of aircraft interior components under crash loads. *International Journal of Crashworthiness* 13 (5):511–21. doi:10.1080/13588260802221203.

Hexcel. 1999. *HexWeb: Honeycomb attributes and properties: A comprehensive guide to standard Hexcel honeycomb materials, configurations, and mechanical properties*. Stamford, CT: Hexcel Composite. http://www.hexcel.com/user_area/uploads/Honeycomb_Attributes_and_Properties.pdf.

Hu, L. L., F. F. You, and T. X. Yu. 2011. Crushing strength of honeycombs with various cell wall angles. *Materials Research Innovations* 15 (sup1):s155–s157. doi:10.1179/143307511X12858956847912.

Hu, L., F. You, and T. Yu. 2013. Effect of cell-wall angle on the in-plane crushing behaviour of hexagonal honeycombs. *Materials & Design* 46:511–23. doi:10.1016/j.matdes.2012.10.050.

Ivañez, I., L. M. Fernandez-Cañadas, and S. Sanchez-Saez. 2017. Compressive deformation and energy-absorption capability of aluminium honeycomb core. *Composite Structures* 174:123–33. doi:10.1016/j.compstruct.2017.04.056.

Jen, Y. M., and L. Y. Chang. 2009. Effect of thickness of face sheet on the bending fatigue strength of aluminum honeycomb sandwich beams. *Engineering Failure Analysis* 16 (4):1282–93. doi:10.1016/j.engfailanal.2008.08.004.

Kolb, G. J., C. H. Ho, T. R. Mancini, and J. A. Gary. 2011. Power tower technology roadmap and cost reduction plan. Report No. SAND2011-2419. Sandia National Laboratories, Albuquerque, NM. http://prod.sandia.gov/techlib/access-control.cgi/2011/112419.pdf.

Kolb, G., S. Jones, M. Donnelly, D. Gorman, R. Thomas, R. Davenport, and R. Lumia. 2007. Heliostat cost reduction study. Report No. SAND2007-3293. Sandia National Laboratories, Albuquerque, NM. http://prod.sandia.gov/techlib/access-control.cgi/2007/073293.pdf.

Lande, P. R., and R. V. Patil. 2015. Analysis of bumper beam in frontal collision. *International Journal of Innovative Research in Science* 4:2807–10.

Langdon, G. S., G. N. Nurick, M. Y. Yahya, and W. J. Cantwell. 2010. The response of honeycomb core sandwich panels, with aluminum and composite face sheets, to blast loading. *Journal of Sandwich Structures & Materials* 12 (6):733–54. doi:10.1177/1099636210368470.

Lee, K., Z. Huque, R. Kommalapati, and S. E. Han. 2017. Fluid-structure interaction analysis of NREL phase VI wind turbine: Aerodynamic force evaluation and structural analysis using FSI analysis. *Renewable Energy* 113:512–31. doi:10.1016/j.renene.2017.02.071.

Li, Q. Q., E. Li, T. Chen, L. Wu, G. Q. Wang, and Z. C. He. 2021. Improve the frontal crashworthiness of vehicle through the design of front rail. *Thin-Walled Structures* 162:107588. doi:10.1016/j.tws.2021.107588.

Liedke, P., A. Pfahl, J. F. Vásquez-Arango, and E. Hölle. 2018. 3rd generation rim drive heliostat with monolithic sandwich panel. *AIP Conference Proceedings* 2033 (1):040021.

Lin, C.-K., C.-Y. Dai, and J.-C. Wu. 2013. Analysis of structural deformation and deformation-induced solar radiation misalignment in a tracking photovoltaic system. *Renewable Energy* 59:65–74. doi:10.1016/j.renene.2013.03.031.

MacPhee, D., and A. Beyene. 2013. Fluid-structure interaction of a morphing symmetrical wind turbine blade subjected to variable load. *International Journal of Energy Research* 37 (1):69–79. doi:10.1002/er.1925.

Mammar, M., S. Djouimaa, A. Hamidat, S. Bahria, and M. El Ganaoui. 2017. Wind effect on full-scale design of heliostat with torque tube. *Mechanics & Industry* 18 (3):312. doi:10.1051/meca/2016059.

Mancini, T. R. 2000. Catalog of solar heliostats. SolarPACES report No. III-1/00. http://www.fika.org/jb/resources/Heliostat%20Catalog.pdf.

Marais, M. D., K. J. Craig, and J. P. Meyer. 2015. Computational flow optimization of heliostat aspect ratio for wind direction and elevation angle. *Energy Procedia* 69:148–57. doi:10.1016/j.egypro.2015.03.018.

Nast, E. 1997. On Honeycomb-Type Core Moduli. Presented at the Collection of Technical Papers-AIAA/ASME/ASCE/AHS/ASC Structures, Structural Dynamics and Materials Conference, 2, 1035–44.

Nayak, S. K. 2012. Design optimization of honeycomb sandwich panels for blast load mitigation. Doctoral dissertation, The Pennsylvania State University, United States. OECD Publication, France.

Paik, J. K., A. K. Thayamballi, and G. S. Kim. 1999. The strength characteristics of aluminum honeycomb sandwich panels. *Thin-Walled Structures* 35 (3):205–31. doi:10.1016/S0263-8231(99)00026-9.

Palomba, G., G. Epasto, and V. Crupi. 2021. Lightweight sandwich structures for marine applications: A review. *Mechanics of Advanced Materials and Structures* 2021:1–26. doi:10.1080/15376494.2021.1941448.

Peterka, J. A., and R. G. Derickson. 1992. Wind load design methods for ground-based heliostats and parabolic dish collectors. Report number SAND92-7009. Sandia National Laboratories, Albuquerque, NM.

Peterka, J. A., N. Hosoya, B. Bienkiewicz, and J. E. Cermak. 1986. Wind load reduction for heliostats. Report SERI/STR-253-2859. Solar Energy Research Institute, Golden, CO. https://www.nrel.gov/docs/legosti/old/2859.pdf.

Pfahl, A., J. Coventry, M. Röger, F. Wolfertstetter, J. F. Vásquez-Arango, F. Gross, M. Arjomandi, P. Schwarzbözl, M. Geiger, and P. Liedke. 2017. Progress in heliostat development. *Solar Energy* 152:3–37. doi:10.1016/j.solener.2017.03.029.

Pfahl, A., M. Buselmeier, and M. Zaschke. 2011. Wind loads on heliostats and photovoltaic trackers of various aspect ratios. *Solar Energy* 85 (9):2185–201. doi:10.1016/j.solener.2011.06.006.

Redmann, A., M. C. Montoya-Ospina, R. Karl, N. Rudolph, and T. A. Osswald. 2021. High-force dynamic mechanical analysis of composite sandwich panels for aerospace structures. *Composites Part C: Open Access* 5:100136. doi:10.1016/j.jcomc.2021.100136.

Rumsey-Hill, N., J. Pottas, and J. Coventry. 2019. Design of efficient stamped mirror facets using topography optimisation. *AIP Conference Proceedings* 2126 (1):030048.

Schwingshackl, C. W., G. S. Aglietti, and P. R. Cunningham. 2006. Determination of honeycomb material properties: Existing theories and an alternative dynamic approach. *Journal of Aerospace Engineering* 19 (3):177–83. doi:10.1061/(ASCE)0893-1321(2006)19:3(177).

Shifa, M., F. Tariq, and A. D. Chandio. 2021. Mechanical and electrical properties of hybrid honeycomb sandwich structure for spacecraft structural applications. *Journal of Sandwich Structures & Materials* 23 (1):222–40. doi:10.1177/1099636219830783.

Sorohan, Ş., D. M. Constantinescu, M. Sandu, and A. G. Sandu. 2016. Assessment of effective elastic properties of honeycomb cores by modal finite element analyses. Proceedings of the European Automotive Congress EAEC-ESFA 2015, 443–54.

Staal, R. A., G. D. Mallinson, K. Jayaraman, and D. P. W. Horrigan. 2009. Predicting failure loads of impact damaged honeycomb sandwich panels. *Journal of Sandwich Structures & Materials* 11 (2-3):213–44. doi:10.1177/1099636208103554.

Strachan, J. W., and R. M. Houser. 1993. Testing and evaluation of large-area heliostats for solar thermal applications. Report No. SAND92-1381. SANDIA Labs, Alburquerque, NM. http://energy.sandia.gov/wp-content/gallery/uploads/SAND92_1381_heliostat_testing.pdf.

Téllez, F., M. Burisch, C. Villasente, M. Sánchez, C. Sansom, P. Kirby, P. Turner, C. Caliot, A. Ferriere, C. A. Bonanos, et al. 2014. State of the art in heliostats and definition of specifications: Survey for a low cost heliostat development. STAGE-STE Project Report.

Totten, G. E., M. Tiryakioglu, and O. Kessler. 2018. *Encyclopedia of aluminum and its alloys*. 1st ed. Boca Raton, FL: CRC Press.

Wang, L., R. Quant, and A. Kolios. 2016. Fluid structure interaction modelling of horizontal-axis wind turbine blades based on CFD and FEA. *Journal of Wind Engineering and Industrial Aerodynamics* 158:11–25. doi:10.1016/j.jweia.2016.09.006.

Wu, Z., B. Gong, Z. Wang, Z. Li, and C. Zang. 2010. An experimental and numerical study of the gap effect on wind load on heliostat. *Renewable Energy* 35 (4):797–806. doi:10.1016/j.renene.2009.09.009.

Yamashita, M., and M. Gotoh. 2005. Impact behavior of honeycomb structures with various cell specifications—numerical simulation and experiment. *International Journal of Impact Engineering* 32 (1–4):618–30. doi:10.1016/j.ijimpeng.2004.09.001.

Zenkert, D. 1997. *The handbook of sandwich construction*. West Midlands, UK: EMAS Ltd.

Appendix A

Determining a proper size for the sandwich panel's supporting steel attachments that minimizes the overall weight of the mirror support structure (in comparison to the support structure of the existing 148 m^2 steel-based ATS heliostat that weighs around 1550 kg (Kolb et al. 2007)) while maintaining its structural integrity requires investigating the effect of attachment sizes on the heliostat panel's structural behavior. Different attachment sizes were tested (Figure 24) to check their effects on the heliostat surface's maximum recorded displacement when the structure is tilted at an angle of 30° and experiencing wind at 0° incidence angle with a velocity of 20 m/s.

As can be seen from Figure 24, which demonstrates the displacement and weight reduction percentage variations at various attachment sizes, as one may expect, increasing the size of the attachment reduces the recorded maximum displacement values significantly. However, this improvement comes with a major decrease in the

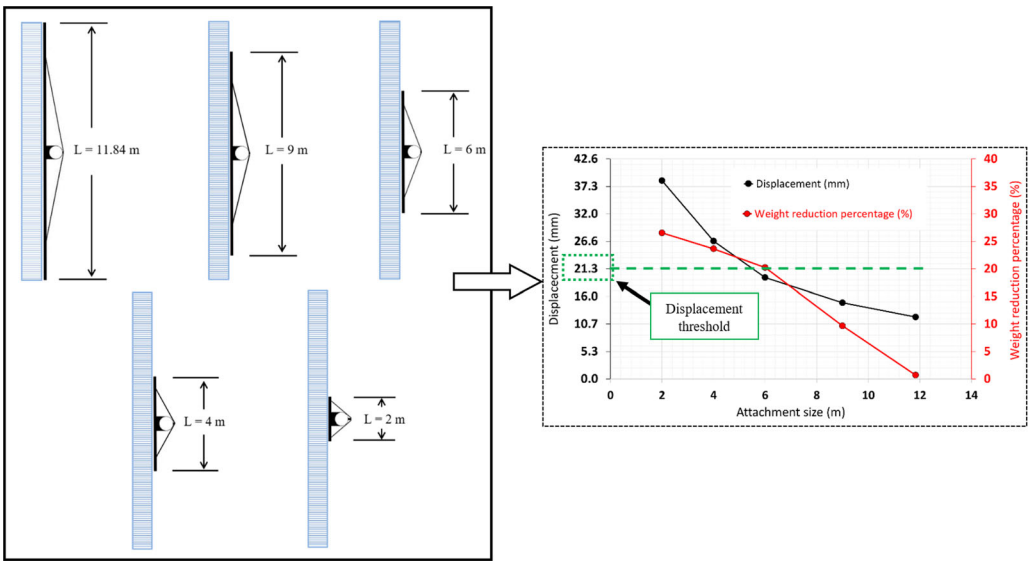

Figure 24. Attachment sizes investigated in the study.

attained weight reduction. For reliable operation of a heliostat, the structure should be able to keep its deformation below 21.3 mm (as derived from Björkman's (Björkman 2014) approach of calculating the maximum allowable displacement) such that the acceptance angle loss of its reflective surface resides within tolerable limits. From the results, it is clear that the most desirable tradeoff between the heliostat panel's structural deformation and attained weight reduction is when the panel is supported by attachments with a length of around 6 m, hence the 6 m attachment size was selected for further FSI analysis.

Appendix B

Nomenclature

t	Sheet thickness
a	Cell wall length
φ	Core angle
E	Young's modulus of the honeycomb's solid material
v	Poisson's ratio of the honeycomb's solid material
G	Shear modulus of the honeycomb's solid material
ρ	Density of the honeycomb's constituent material
E_1	Young's modulus of the honeycomb core in direction 1
E_2	Young's modulus of the honeycomb core in direction 2
E_3	Young's modulus of the honeycomb core in direction 3
v_{12}	Poisson's ratio of the honeycomb core in plane 1–2
v_{23}	Poisson's ratio of the honeycomb core in plane 2–3
v_{13}	Poisson's ratio of the honeycomb core in plane 1–3
G_{12}	Shear modulus of the honeycomb core in plane 1–2
G_{23}	Shear modulus of the honeycomb core in plane 2–3
G_{13}	Shear modulus of the honeycomb core in plane 1–3
$\rho_{\text{honeycomb}}$	Density of the honeycomb core

$$E_1 = \frac{t^3(1+\sin\varphi)}{12\ a^3\cos^3\varphi\left[\frac{\cos\varphi}{3}-\frac{1+\cos\varphi}{8}\right](1-v^2)}\,E \tag{1}$$

$$E_2 = \frac{t^3\cos\varphi}{(1+\sin\varphi)\ a^3\sin^2\varphi\,(1-v^2)}\,E \tag{2}$$

$$E_3 = \frac{2\,t}{a\cos\varphi(1+\sin\varphi)}\,E \tag{3}$$

$$G_{12} = \frac{t^3(1+\sin\varphi)}{a^3\,(1-v^2)\cos\varphi(6.25-6\sin\varphi)}\,E \tag{4}$$

$$G_{23} = \frac{10\,t}{9\ a\ \cos^3\varphi(1+\sin\varphi)}\,G \tag{5}$$

$$G_{13} = \frac{2\,t}{a\cos\varphi(1+\sin\varphi)}\,G \tag{6}$$

$$v_{12} = \frac{\cos^2\varphi}{\sin\varphi(1+\sin\varphi)} \tag{7}$$

$$v_{23} = \frac{t^2\cos^2\varphi}{2\,a^2\sin^2\varphi\,(1-v^2)}\,v \tag{8}$$

$$v_{13} = \frac{t^2\,(1+\sin\varphi)^2}{24\,a^2\cos\varphi\left[\frac{\cos\varphi}{3}-\frac{1+\cos\varphi}{8}\right]} * \frac{v}{(1-v^2)} \tag{9}$$

$$\rho_{\text{honeycomb}} = \frac{3\,t}{2\,a\cos\varphi(1+\sin\varphi)}\,\rho \tag{10}$$